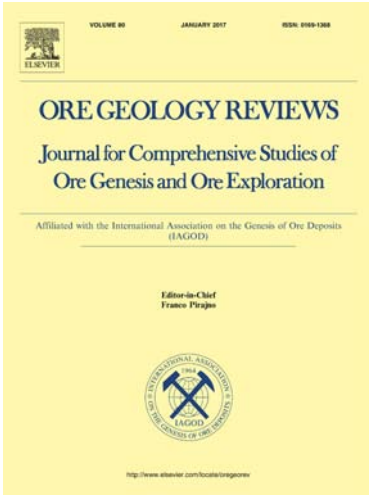

The Cogne magnetite deposit (Western Alps, Italy): a Late Jurassic seafloor ultramafic-hosted hydrothermal system?

Luca Toffolo, Paolo Nimis, Silvana Martin, Simone Tumiati, Wolfgang Bach

PII: S0169-1368(16)30444-9
DOI: http://dx.doi.org/10.1016/j.oregeorev.2016.11.030
Reference: OREGEO 2035

To appear in: *Ore Geology Reviews*

Received Date: 26 July 2016
Revised Date: 23 November 2016
Accepted Date: 24 November 2016

Please cite this article as: L. Toffolo, P. Nimis, S. Martin, S. Tumiati, W. Bach, The Cogne magnetite deposit (Western Alps, Italy): a Late Jurassic seafloor ultramafic-hosted hydrothermal system?, *Ore Geology Reviews* (2016), doi: http://dx.doi.org/10.1016/j.oregeorev.2016.11.030

The Cogne magnetite deposit (Western Alps, Italy): a Late Jurassic seafloor ultramafic-hosted hydrothermal system?

Luca Toffolo[1,*], Paolo Nimis[1], Silvana Martin[1], Simone Tumiati[2], Wolfgang Bach[3]

[1] Geosciences Department, University of Padua, via Gradenigo 6, 35100 Padua, Italy, luca.toffolo@phd.unipd.it, paolo.nimis@unipd.it, silvana.martin@unipd.it

[2] Earth Sciences Department, University of Milan, via Mangiagalli 34, 20133 Milan, Italy, simone.tumiati@unimi.it

[3] Department of Geosciences and MARUM Center for Marine Environmental Sciences, P.O. Box 330440, 28334 Bremen, Germany, wbach@uni-bremen.de

* Corresponding author.

ABSTRACT

The Cogne magnetite deposit (Western Alps, Italy) is the largest in a series of apatite and sulphide-free magnetite orebodies that are hosted in serpentinites belonging to western Alpine ophiolitic units. The nearly endmember composition of magnetite, which is unusual for an ultramafic setting, and the relatively high tonnage of the deposit ($18 \cdot 10^6$ tonnes at 45-50 wt% Fe) make Cogne an intriguing case study to explore magnetite-forming processes in ophiolites. The Cogne magnetite shows variable textures, including nodular ores, veins and fine-grained disseminations in serpentinites after tectonitic peridotites and totally serpentinized melt-impregnated peridotites (troctolites). An increase in Co/Ni ratio from magnetite-poor serpentinized peridotites (0.05) to nodular magnetite ores (>1) is observed. Trace element analyses of magnetite from different sites and lithologies by laser-ablation inductively-coupled mass spectrometry indicate that magnetites

have typical hydrothermal compositions, characterized by high Mg and Mn (median values up to ~24100 and ~5000 ppm, respectively), and low Cr, Ti and V (median values up to ~30, ~570 and ~60 ppm, respectively). Moreover, the variations in trace element compositions distinguish magnetite that is hydrothermal fluid-controlled [highest (Mg, Mn, Co, Zn)/Ni ratios] from magnetite whose composition is affected by host-rock chemistry (highest Ni ± Ti ± V). U-Th-Pb dating of magnetite-associated uraninite constrains the formation of the deposit to the Late Jurassic (ca. 150 Ma), during an advanced stage of the opening of the Alpine Tethys. Thermodynamic modelling of fluid-rock interactions indicates that fluids produced by seawater–peridotite or seawater–Fe-gabbro are not sufficiently Fe-rich to account for the formation of the Cogne deposit. This suggests that fractionation processes such as phase separation were critical to generate hydrothermal fluids capable to precipitate large amounts of magnetite in various types of ultramafic host-rocks. The oceanic setting and geochemical and mineralogical similarities with some modern ultramafic-hosted volcanogenic massive sulphide deposits on mid-ocean ridges suggest that the exposed mineralized section at Cogne may represent the deep segment of a seafloor, high-temperature (~300–400°C) hydrothermal system. The occurrence of similar magnetite enrichments in present-day oceanic settings could contribute to explain the presence of significant magnetic anomalies centred on active and inactive ultramafic-hosted hydrothermal fields.

1. Introduction

The Cogne mining district (southern Valle d'Aosta region, Western Alps, Italy; Fig. 1) consists of a set of mines, which exploited a magnetite-rich serpentinite unit from the Middle Ages to 1979. The tonnage of the ore deposit was estimated at 18 Mt (Nazionale "Cogne" S.p.a., 1954), and the run-of-mine ore produced in the 1960s had an iron grade of 45-50% (Di Colbertaldo et al., 1967). The Cogne deposit is the largest in a series of apatite and sulphide-free serpentinite-hosted magnetite orebodies that crop out in ophiolitic units along the western Alpine collisional suture in Valle d'Aosta (Castello, 1981; Diella et al., 1994; Rossetti et al., 2009; Stella, 1921) and in its southern extension in Corsica (Farinole mine; Routhier, 1963). In southern Valle d'Aosta, most of these magnetite orebodies occur in the Mt. Avic serpentinite massif (located ca. 15 km ENE of the Cogne serpentinite; Fig. 1) and have been interpreted as former metasomatized podiform chromitites, based on their high Cr concentration and the presence of chromite relicts (Diella et al., 1994; Della Giusta et al., 2011; Rossetti et al., 2009). A similar origin has been proposed for analogous Mesozoic (probably Jurassic), ophiolite-hosted magnetite deposits in Greece (Vermion, Olympus and Edessa regions and Skyros island; Paraskevopoulos and Economou, 1980). The Cogne deposit differs from the above occurrences because its magnetite has a nearly pure endmember composition and contains only trace amounts of compatible elements such as Cr, Ti and V (Carbonin et al., 2014; Compagnoni et al., 1981). This geochemical fingerprint, which is unusual for an ultramafic setting, as well as the relatively high tonnage of the deposit, make Cogne an interesting and still poorly studied example of ophiolite-hosted magnetite deposit. Understanding its genesis may have implications for our interpretation of magnetic anomalies reported from modern ultramafic-hosted hydrothermal sites on slow-spreading mid-ocean ridges (Fujii et al., 2016; Szitkar et al., 2014; Tivey and Dyment, 2010).

Several hypotheses have been put forward to explain the genesis of the Cogne deposit. Di Colbertaldo et al. (1967) proposed a genesis by magmatic segregation from an ultramafic melt.

Based on the Cr and Ti-poor composition of the magnetite, Compagnoni et al. (1979, 1981) ascribed the formation of the Cogne magnetite to high-temperature serpentinization of oceanic peridotites and consequent Fe mobilization, but they did not discuss this hypothesis in detail. Recently, Carbonin et al. (2014) investigated some of the magnetite-associated lithologies and suggested their possible hydrothermal origin; however, the ore-forming processes were not explored.

In this paper, we present new petrographic and geochemical data on the Cogne deposit, focusing on the textural relationships and the trace element composition of magnetite. The latter has been a valuable tool in the identification of the petrogenetic environment (e.g., Boutroy et al., 2014; Dare et al., 2014; Dupuis and Beaudoin, 2011; Nadoll et al., 2014; Nadoll et al., 2015). In addition, we determine for the first time the radiometric age of the magnetite orebody by U–Th–Pb dating of uraninite. We will show that the magnetite geochemistry and age support a seafloor oceanic hydrothermal setting for the Cogne deposit, and we will explore the possible formation mechanisms, using constraints from geochemical modelling of seawater-rock reactions.

2. Geology of the Cogne mining area

The Cogne serpentinite is a 2.5 km long sliver, with an average thickness of 100 m (Di Colbertaldo et al. 1967), which is exposed on the S and W slopes of Montzalet (Fig. 1 and 2). The serpentinite is tectonically sandwiched between two different metasedimentary sequences. The foot wall sequence consists of tectonically juxtaposed slivers of calcschists, marbles, dolomitic marbles and quartzites formed in a continental margin and in other paleogeographic domains (Cogne Unit; Polino et al., 2014). The hanging wall sequence is represented by calcschists, marbles and minor, Fe- and Mn-bearing metacherts. The basal contact of the serpentinite is a thrust fault (Elter, 1971), while the upper limit is marked by a few cm- to 3 m-thick boudinaged rodingite, which we tentatively interpret as a tectonically activated, primary serpentinite-sediment interface. According to Elter

(1971), the Cogne serpentinite and the hanging wall metasediments form the core of a km-scale isoclinal fold that repeats the Cogne unit in its upper limb (Fig. 2b). The Cogne serpentinite and the hanging wall metasediments are considered to be part of the same greenschist- to blueschist-facies ophiolite-bearing unit (Aouilletta Unit; Polino et al., 2014), which is sandwiched together with the foot wall marbles and quartzites between two eclogite-facies ophiolitic units (Grivola-Urtier Unit and Zermatt-Saas Unit; Dal Piaz et al., 2010). These ophiolitic units are remnants of the Jurassic Piedmont-Liguria ocean (Alpine Tethys; Schmid et al., 2004; Stampfli, 2000). From Late Cretaceous to Eocene, these ophiolitic units followed different P-T paths related to their subduction beneath the Adriatic micro-plate, as a result of Africa-Europe convergence (Schmid et al., 2004). In the Zermatt-Saas Unit (in southern Valle d'Aosta), the high-pressure (eclogitic) metamorphic peak was reached in the Eocene (45-42 Ma; Dal Piaz et al., 2001), contemporaneously with the closure of the ocean (Dal Piaz et al., 2003), and was followed by a greenschist-facies overprint during Late Eocene-Early Oligocene (Dal Piaz et al., 2001, 2003). No P-T-time estimate is available for the Cogne serpentinite and its host Aouilletta Unit.

The Cogne magnetite mineralization is confined to the serpentinite body (Compagnoni et al., 1979; Di Cobertaldo et al., 1967) and it is exposed in three zones, henceforward referred to as Site 1, Site 2 and Site 3 (Fig. 2). At Site 1 (which includes the mines of Liconi, 45.612509 N 7.395377 E, Colonna, 45.609716 N 7.391322 E, and Costa del Pino, 45.610466 N 7.378247 E), the orebody is a 50-70 m-thick, 600 m-long continuous lens that dips and wedges out northward (Di Colbertaldo et al., 1967). This orebody was extensively exploited in the second half of the twentieth century by sublevel caving. At Site 2 (western slope of Montzalet, 45.618124 N 7.386316 E) and Site 3 (Larsinaz mine, 45.619119 N 7.377135 E), the intensely mineralized rock volumes are much smaller, and consist of disseminations and veins at Site 2 and of a less than 10 m-thick lens at Site 3 (Stella, 1916). The mineralized serpentinite was subjected to only low degrees of Alpine deformation and metamorphism (Carbonin et al., 2014), which allowed extensive preservation of the original structures (see below).

3. Materials and methods

3.1. Petrographic and mineralogical analysis

Sixty-eight rock samples from the Cogne mining area were collected from mine dumps and outcrops and studied by means of optical microscopy in thin polished sections. No potential source of lead was present during any stage of the sample preparation, to avoid contamination that could invalidate the subsequent geochronological analyses. Mineral identification was aided by micro-Raman spectroscopy, using a Thermo Scientific™ DXR™ confocal Raman system at the Chemistry Department of the University of Padua (Italy). We chose a 532 nm laser working at a power of 5-10 mW. All of the Raman spectra were collected with a 50x LWD objective lens, reaching a spatial resolution of ~1 μm. Raman spectroscopy was crucial for the identification of serpentine minerals, for which we followed the guidelines by Groppo et al. (2006) and Carbonin et al. (2014). Selected samples were further investigated using a scanning electron microscope (SEM). Back-scattered electron images were obtained using a CamScan MX 2500 SEM at the Department of Geosciences of the University of Padua (Italy) equipped with a LaB_6 crystal, working at 20 kV accelerating voltage and 140 nA current.

Mineral compositions of major minerals were determined by electron microprobe analysis (EPMA) using a CAMECA SX-50 electron microprobe, equipped with four WDS spectrometers and one EDS spectrometer, at IGG-CNR, Padua (Italy). The Kα emission lines of ten elements (Na, Mg, Al, Si, K, Ca, Ti, Cr, Mn, Fe) were measured using the following natural and synthetic minerals and oxides as standards: albite (Na), diopside (Si, Ca), orthoclase (K), MgO, Al_2O_3, $MnTiO_3$, Cr_2O_3 and Fe_2O_3. Working conditions were 20 kV, 20 nA, 10 s for peak and 5 s for the background on each side of the peak.

149

150 *3.2. Bulk rock compositions*

151

152 Fourteen rock samples, representative of the main lithologies encountered in and around the
153 deposit, were analysed for major, minor and selected trace elements by X-ray fluorescence (XRF).
154 The samples were prepared as fine powder by means of a Retsch M0 agate mortar grinder and a
155 Retsch RS100 vibratory disk mill, equipped with agate disks. The powder samples, fused into
156 beads, were then analysed using a Philips PW2400 XRF wavelength-dispersive sequential
157 spectrometer equipped with a Rh tube at the Department of Geosciences of the University of Padua
158 (Italy). Reference standards were natural geological samples (Govindaraju, 1994). The relative
159 analytical precision is estimated to within ±0.6% for major and minor elements and within ±3% for
160 trace elements. The relative accuracy is within ±0.5% for Si, ±3% for the other major and minor
161 elements, and ±5% for trace elements. Detection limits are better than 0.01 wt% for Al, Mg and Na,
162 0.2 wt% for Si and 0.005 wt% for Ti, Fe, Mn, Ca, K and P. For trace elements, the detection limits
163 are 3 ppm for Co, Ni, Cu, Zn, Rb, Sr, Y, Zr, Nb, Th, and U, 5 ppm for Sc, V, Ga, and Pb, 6 ppm for
164 Cr, and 10 ppm for Ba, La, Ce, and Nd.

165 The geochemistry of seven whole-rock samples was further investigated by inductively coupled
166 plasma mass spectrometry and emission spectroscopy (ICP-MS/ES) analyses, which were
167 performed by Bureau Veritas Mineral Laboratories (Canada). The pulverised rock samples were
168 mixed with $LiBO_2/Li_2B_4O_7$ flux and fused. The cooled beads were then digested with ACS grade
169 nitric acid. The detection limits for trace elements are: 1 ppm for Be, Sc, Sn, and Ba; 8 ppm for V;
170 14 ppm for Cr; 0.2 ppm for Co and Th; 20 ppm for Ni; 0.5 ppm for Ga, Sr and W; 0.1 ppm for Y,
171 Zr, Nb, Cs, Hf, Ta, U, La, Ce; 0.3 ppm for Nd.

172

173 *3.3. U-Th-Pb dating*

174

Thirteen thin sections of magnetite ore were scanned for uraninite crystals by back-scattered electron imaging with a Scanning Electron Microscope (SEM). Four of these samples showed uraninite grains of sufficient size to allow their chemical analysis by EPMA and successive dating by the U-Th-Pb method. Uraninite compositions were measured at the Department of Earth Sciences of the University of Milan (Italy), using a JEOL JXA-8200 electron microprobe equipped with five WDS and one EDS spectrometers. An accelerating voltage of 15 kV and a beam current intensity of 20 nA were used. Nine elements were measured by WDS spectrometry using the following X-ray lines: Mg$K\alpha$, Si$K\alpha$, Ti$K\alpha$, Ca$K\alpha$, Cr$K\alpha$, Fe$K\alpha$, U$M\beta$, Th$M\alpha$ and Pb$M\alpha$. The counting time was 60 s for the peak and 30 s for the background for all analysed elements. The standards were olivine (Mg), grossular (Si and Ca), ilmenite (Ti), fayalite (Fe), pure Cr and synthetic UO_2, ThO_2 and PbO. Detection limits for elements relevant to geochronology are 290 ppm for U, and 170 ppm for Th and Pb. Relative errors (relative standard errors) of 0.1%, 0.5% and 0.7% for U, Th and Pb concentrations, respectively, were calculated on the basis of 5 repetitions of the same measurement. However, a more realistic minimum relative error for U, Th and Pb concentrations >7500 ppm is 2% (Cocherie and Albarede, 2001).

Chemical maps were preliminarily acquired on the uraninite grains to assess the presence of chemical zoning. In order to collect a significant amount of data, we performed both single spot analyses and automated traverses. The latter method allowed us to obtain a large number of data points, although the proportion of mixed or poor-quality analyses increased. Thus, prior to calculating ages, we excluded the analyses which showed obvious contaminations, low totals or anomalously low Pb contents, if compared to adjacent points in the same traverse.

The possibility of dating uraninite with EPMA was discussed by Bowles (1990) and calculated ages were demonstrated to be accurate and consistent with independent isotopic measurements (Bowles, 2015; Cross et al., 2011). According to Bowles (2015), the best accuracy is obtained for ages from ~2 Ma to 700-1000 Ma: the lower limit is imposed by the EPMA detection limit of Pb and the upper limit is linked to metamictization of the uraninite crystal lattice, which may lead to Pb

loss. Meaningful ages are obtained if the initial concentration of non-radiogenic Pb is negligible and the U-Th-Pb system remained closed after uraninite crystallization. The former assumption is considered to hold true because Pb^{2+} is incompatible in the uraninite crystal structure (Alexandre and Kyser, 2005), whereas the latter assumption needs to be assessed by careful sample examination.

The formula used to calculate the age *t* (in years) is (Montel et al., 1996):

$$Pb = 208(Th/232) \cdot [\exp(\lambda^{232} \cdot t) - 1] + 206(U/238.04) \cdot [1 - (^{235}U/^{238}U)] \cdot [\exp(\lambda^{238} \cdot t)] +$$

$$+ 207(U/238.04) \cdot (^{235}U/^{238}U)] \cdot [\exp(\lambda^{235} \cdot t)],$$

where Th and U are the measured concentrations in ppm, λ^{232}, λ^{238}, λ^{235} are the decay constants of ^{232}Th, ^{238}U and ^{235}U, respectively, and $^{235}U/^{238}U$ is the bulk Earth's uranium isotopic ratio. The values used in the calculations are: $\lambda^{232} = 4.9475 \cdot 10^{-11}$ a^{-1} (LeRoux and Glendenin, 1963); $\lambda^{238} = 1.55125 \cdot 10^{-10}$ a^{-1} and $\lambda^{235} = 9.8485 \cdot 10^{-10}$ a^{-1} (Jaffey et al., 1971); $^{235}U/^{238}U = 0.0072559$ (Hiess et al., 2012). To obtain an initial guess of *t* we used the formula (modified from Bowles, 2015):

$$t = (1/\lambda^{238}) \cdot \ln (1 + Pb/\{[1 - (^{235}U/^{238}U)] \cdot 206(U/238.04)\}).$$

Then the difference between the calculated and the measured values of Pb is minimized by least-squares method, varying *t*. Whenever possible, ages were obtained as weighted averages of several analyses, after outlier rejection based on a modified 2σ set of criteria (Ludwig, 2012).

3.4. Trace elements in magnetite

Trace elements in magnetite were measured by laser-ablation inductively-coupled plasma mass spectrometry (LA-ICP-MS) at the Petrology of the Ocean Crust Laboratory, University of Bremen (Germany), using a high-resolution double-focussing ThermoFinnigan Element2, equipped with a solid-state laser with a wavelength of 193 nm (New Wave UP193). Magnetite grains were analysed on standard thin polished sections using a 35 μm laser spot size, a pulse frequency of 5 Hz, an

226 irradiance at the sample of ~1.3 GW/cm^2 and an acquisition time of 60 s, comprehensive of 25 s for
227 background measurement. To avoid any risk of contamination on the surface of the rock section, the
228 zone to be investigated was pre-ablated using two laser pulses with 50 μm spot size. The analysed
229 elements (^{25}Mg, ^{29}Si, ^{43}Ca, ^{47}Ti, ^{51}V, ^{53}Cr, ^{55}Mn, ^{57}Fe, ^{59}Co, ^{60}Ni, ^{66}Zn, ^{90}Zr, ^{98}Mo) were measured
230 in low-resolution mode in order to shorten the acquisition time, although preserving high counts per
231 second (cps). We opted for this configuration to avoid deep ablation pits, thus reducing the
232 probability of hitting inclusions or adjacent minerals. The Fe concentration of magnetite as
233 determined by EPMA was used as an internal standard. External standards (reference materials
234 NIST61, BCR-2G and BHVO) were analysed under the same conditions as the samples every 5 to 9
235 analyses during the same session, in order to check for possible drift. Signal files, reporting
236 intensities (cps) vs. time, were inspected for possible heterogeneities related to the presence of
237 inclusions and chemical zoning. Integration of the signal and calculation of concentrations were
238 performed with the GeoPro™ software (CETAC Technologies). Detection limits (DL) were
239 calculated on reference materials using the formula:
240 $DL_i = [3\sqrt{2}s_{bkgd}/(\bar{X}_{sgl} - \bar{X}_{bkgd})] \cdot C_i$,
241 where i is the ith element, s_{bkgd} is the sample standard deviation of the background (in cps), $\bar{X}_{sgl}$ and
242 $\bar{X}_{bkgd}$ are the average signal and the background (in cps) respectively, and C_i is the concentration (in
243 ppm) of the ith element in the reference materials.
244 The statistical relationships between chemical elements in magnetite were explored by robust
245 principal component analysis (PCA), using the function "pcaCoDa" in the "robCompositions"
246 library for R software (Templ et al., 2011). Robust PCA was preferred to "classical" PCA because it
247 is less sensible to outliers (Filzmoser et al., 2009; Filzmoser and Hron, 2011). Four analyses (out of
248 ninety-four) with V contents below the detection limit were excluded from calculations.
249
250 *3.5. Geochemical modelling*
251

In an attempt to simulate the genesis of the Cogne deposit in a seafloor hydrothermal model system, fluid-rock interactions were modelled with the EQ3/6 (Version 8.0a) software package (Wolery, 2013), using the database compiled by Klein et al. (2009), which contains thermodynamic properties of minerals and solutes in the 0-400°C range at the fixed pressure of 500 bar. The database was modified to include revised data for $HCl_{(aq)}$ (Ho et al., 2001), $NaCl_{(aq)}$ (Ho et al., 1994), $KCl_{(aq)}$ (Ho et al., 2000), $FeCl_{2(aq)}$ and $FeCl^{+}_{(aq)}$ (Ding and Seyfried, 1992). The modelling procedure, which in the first steps follows that of Klein et al. (2009), is described below.

First, 1 kg of modern seawater (Table 1; composition from Klein et al., 2009) is speciated at 25°C and 1 bar. Then, seawater is heated and reacted with 1 g of fresh harzburgite (Table 2) in a closed system to the desired temperature (at P = 500 bar), to simulate a downward fluid path towards the reaction zone (Klein et al., 2009). The chosen pressure of 500 bar simulates conditions at ~2000 m below seafloor, which do not exceed the reported depth of magma chambers fuelling hydrothermal fields on slow-spreading ridges (~3 km; Singh et al., 2006), assuming a 3000-m water column, which is a typical value for modern slow-spreading ridge hydrothermal systems (Edmonds, 2010). All the produced minerals are removed at the end of the run, because in a real fluid pathway they would be left behind by downwelling seawater. A positive effect of this step is to narrow down the f_{O_2} range in following calculations, thus improving the code stability (Wolery and Jarek, 2003). In the successive step, which simulates a reaction zone, 1 kg of the resulting hydrothermal fluid is reacted at 400°C with an increasing amount of either fresh harzburgite or Fe-gabbro (Table 2) in a closed system (Wolery and Jarek, 2003). We chose the temperature of 400°C because it maximizes Fe solubility, which is strongly temperature-dependent (Seyfried et al., 2004), and is also compatible with estimates of fluid temperatures in modern subseafloor reaction zones (T >375°C, Berndt et al., 1989; T ~ 400°C based on the maximum amount of heat that water can carry by buoyancy-driven advection, Jupp and Schultz, 2004 and references therein) and with measured temperatures of modern seafloor vent fluids (e.g., Edmonds, 2010). The reaction path is terminated after the maximum value of dissolved Fe is reached. Finally, the Fe-rich hydrothermal fluid is

titrated in a closed system with selected lithologies (Table 2) at 300°C or 400°C, in accordance with the temperature range estimated for hydrothermal mineral assemblages by Carbonin et al. (2014). The equilibrium mineral assemblages and the relative abundances of the phases obtained for different water/rock (W/R) ratios are then compared to those observed in the natural rocks. The model does not account for solid solutions, hence, by suppressing Fe-Mg exchange in secondary phases, it maximises the extent of magnetite production.

4. Results

4.1. Petrographic features of the magnetite ores and mineral compositions

The Cogne magnetite ore is heterogeneous in terms of texture and gangue mineral assemblage. Three main textural types of magnetite ore are distinguished, which are termed here *nodular, fine-grained disseminated* and *vein*.

The nodular ores (Fig. 3a, b) are characterized by mm to cm-sized magnetite crystals in a silicate matrix, giving the rock a macroscopic appearance similar to that of nodular chromitites. The nodular textures show a continuum between three major subtypes, which are termed here *leopard*, *harrisitic* and *massive* subtype, respectively. In the leopard subtype, the magnetite crystals, which mostly consist of aggregates of subgrains, are subrounded and constitute up to 50 vol% of the rock. In the harrisitic subtype, the magnetite crystals form up to 10 cm-long rods, mimicking the texture shown by dendritic olivine in harrisite. In the massive subtype, the magnetite content is as high as 80-90 vol%, but subrounded crystals similar to those of the nodular ores are still recognizable.

The fine-grained disseminated ores consist of bands in the host-rock, which contain variable proportions of sub-millimetric magnetite grains (up to ~70 vol). The vein ores (Fig. 3c) are cm-

303 thick, dismembered veins composed of magnetite, chalcopyrite and antigorite; the proportion of
304 opaque minerals over the associated silicates is ~50 vol%.

305 Since the distribution of the different ore types is not uniform across the deposit, we will treat
306 each sampling site separately.

307

308 *4.1.1. Site 1*

309 The magnetite orebody lies below magnetite-poor (3-6 vol% Mag) serpentinized tectonitic
310 harzburgites. The harzburgites show a more or less developed foliation, and are characterized by the
311 presence of lizardite + antigorite + magnetite ± talc pseudomorphs after former olivine and
312 orthopyroxene (distinguished based on the presence of mesh and bastite textures, respectively) and
313 relicts of accessory Mg-Al-rich chromite (Table 3). Magnetite is fine-grained (<20 μm) and Cr-
314 bearing (Carbonin et al., 2014). A detailed description of the mineralogy and conditions of
315 subseafloor serpentinization of these rocks was given in Carbonin et al. (2014; T = 200-300°C, log
316 f_{O_2} = –36 to –30, log ΣS = –2 to –1).

317 Only nodular ores can be found at this site (Fig. 3a, b). Independently of the ore texture, the
318 gangue mineral assemblage is fairly uniform and comprises, in the order of decreasing abundance,
319 antigorite, lizardite, forsterite, brucite, clinochlore, carbonates, and Ti-rich chondrodite (Table 3).
320 Antigorite composes more than 90 vol% of the matrix between the magnetite crystals. It usually
321 shows an interlocking texture (average grains size = 150 μm), but it can form euhedral, randomly
322 oriented blades when in contact with lizardite or magnetite, forming indented crystal boundaries
323 with the latter mineral (Fig. 4a). This feature was already described in rocks from the western Alps
324 by Debret et al. (2014), who interpreted it as a prograde dissolution texture produced during Alpine
325 subduction metamorphism; however, the antigorite studied by Debret et al. (2014) generally has
326 higher Fe content (up to 8 wt% FeO) than antigorite at Cogne (mostly <3 wt% FeO). Lizardite
327 forms yellowish aggregates of submicron-sized crystals, which are interstitial between euhedral
328 antigorite and magnetite. The Al_2O_3 content of lizardite (~5 wt%) is systematically higher than that

in antigorite (<1 wt%). Forsterite (Fo_{99}) forms up to 50 μm anhedral crystals, usually arranged into elongated aggregates, which replace and seldom form pseudomorphs after antigorite. The forsterite crystals are often altered to fine-grained antigorite along the rim and the fractures. Brucite is of nearly pure Mg-endmember composition and forms subhedral, tabular crystals up to 200 μm in size. Clinochlore forms tabular crystals and intergrowths with antigorite. These intergrowths probably result from the breakdown of Al-rich lizardite. The carbonates (calcite, magnesite, dolomite) form anhedral patches which include antigorite, brucite and fine-grained (<50 μm) anhedral magnetite. Calcite is the most common carbonate and is also present as late veins. Ti-rich chondrodite forms up to 500 μm, colourless to pale yellow, anhedral crystals, which are sometimes surrounded by a corona of olivine. Rare accessory minerals are xenotime, sphalerite, Ni-bearing linnaeite, pyrrhotite and uraninite.

Magnetite-rich (~25 vol%) diopsidites have also rarely been found. In these peculiar rocks, magnetite is interstitial between mm- to cm-sized diopside crystals and coexists with antigorite, andradite and clinochlore. The assemblage antigorite + andradite appears to replace diopside. Samples of this kind were thoroughly described by Carbonin et al. (2014).

4.1.2. Site 2

At this site, the serpentinized tectonitic peridotite can be either replaced by fine-grained disseminated magnetite or crosscut by cm-thick magnetite + chalcopyrite + antigorite veins. The disseminated and vein ores are deformed and dismembered into lenses by Alpine deformation, which at small scale results in an anastomosing pattern of mm- to cm-spaced cleavage planes. This deformation is associated with dynamic recrystallization of antigorite and magnetite, the latter forming elongated porphyroclasts.

The disseminations occur as cm-sized magnetite-enriched bands in antigorite serpentinite and typically show relict features of the former serpentinized peridotite, i.e., bastites (Fig. 4b) and Mg-Al-rich chromite grains (Fig. 4c, d; Table 3). The Mg-Al-rich chromite grains (Fig. 4d) are anhedral

and fractured. They are irregularly altered along the rims and fractures into Fe-rich (~41 wt% FeO) chromite + fine-grained Cr-rich (~4–6 wt% Cr_2O_3, determined by SEM-EDS) chlorite and are mantled by a continuous rim of Cr-bearing magnetite intergrown with antigorite and minor secondary diopside.

In the vein ores, magnetite forms elongated, millimetric patches with a chalcopyrite core in an antigorite matrix (Fig. 4e). Magnetite shows well developed crystal boundaries towards chalcopyrite, while the contacts to the surrounding antigorite are irregular. The limit between the vein and the host serpentinite is sharp.

In both disseminations and veins, antigorite shows an interlocking texture. When it is in contact to magnetite or lizardite it forms up to 100 μm-long euhedral lamellar crystals, producing typical indented boundaries. A generation of nearly pure diopside (Table 3) always accompanies magnetite mineralization. In magnetite disseminations, diopside forms up to 400 μm-long isolated needles, intergrown with antigorite (Fig. 4c, d), while in the vein ore, it forms rare aggregates of 10-60 μm long crystals disseminated in the vein selvages. From textural relationships, diopside appears to postdate the formation of bastite pseudomorphs after orthopyroxene in the host serpentinite.

4.1.3 Site 3

At this site, the magnetite ores exhibit nodular textures, but only the leopard and massive subtypes are found. Antigorite is commonly the sole gangue mineral, but the leopard subtype can be characteristically enriched in diopside ± chlorite (Fig. 3d, 4f; Table 3). Antigorite shows an interlocking texture or forms euhedral crystals when in contact to magnetite or diopside. Antigorite veins crosscutting diopside crystals have been observed. Diopside has a nearly pure endmember composition. In the leopard ores, it forms a granofels composed of mm- to cm-sized subhedral crystals, which include subhedral millimetric magnetite. A late generation of smaller subhedral crystals (<50 μm) fills the interstices between larger grains. The diopside crystals may show patchy or concentric oscillatory zoning, determined by slight variations in Fe content. Textural

relationships indicate that diopside formed during a late stage of magnetite growth (Fig. 4f), which was then locally overprinted by antigorite. Veins made up of euhedral diopside in a matrix of lizardite ± chlorite are commonly observed. Clinochlore is found in diopside-rich leopard ores and has variable Mg# ratios and Al contents (Table 3): the Al-rich variety is found as large (up to 1 mm) subhedral tabular crystals associated with diopside and magnetite; the Al-poor clinochlore is fine-grained and fills the interstices between larger clinochlore and diopside crystals. Calcite is found as interstitial material between diopside crystals and as late veins. Rare accessory minerals are andradite, uraninite, talc and apatite.

4.1.4. Inclusions in magnetite

The magnetite crystals can be rich in mineral inclusions, which, in the largest poikiloblats, are typically concentrated in their cores (Fig. 4a).

At Site 1, the most common inclusions are clinochlore and brucite lamellae (Table 3, often oriented along magnetite (111), anhedral calcite, anhedral sphalerite, rare anhedral pyrite, rare lizardite and forsterite, and very rare euhedral uraninite and apatite. Antigorite inclusions are often present in the outermost zones of the magnetite crystals. Composite inclusions made up of clinochlore + brucite or, rarely, clinochlore + calcite are also observed.

At Site 2, the most abundant inclusions are euhedral antigorite and anhedral sulphides. The sulphides consist of fine lamellar chalcopyrite–cubanite intergrowths and unmixed "bornite solid solution" grains, composed of lamellar intergrowths of bornite and chalcocite. Also present are pyrrhotite, which shows exsolution of Co-rich pentlandite, and sphalerite. Other minor included minerals are lamellar clinochlore and anhedral andradite.

At Site 3, the inclusions are mainly composed of clinochlore, which can be associated with rare andradite (Table 3) and very rare diopside and uraninite; antigorite inclusions are only present near the rims of the magnetite crystals.

4.2. Petrography of peculiar host rocks at sites 1 and 3

At sites 1 and 3, serpentinites showing a pegmatoid texture are associated with the magnetite ore and can be variably enriched in magnetite. In the barren rocks (Fig. 3e), cm-sized amoeboid domains made of dominant euhedral coarse-grained (50-300 μm) antigorite that replaces yellow, fine-grained (sub-micron sized) lizardite are interweaved with domains composed of mesh textured antigorite + lizardite and very fine-grained magnetite (magnetite I) lining the rims of the mesh. Lizardite is Al-rich in both domains (Raman peak at 382-385 cm^{-1}, indicating Al substitution for Si in the tetrahedral sites; Groppo et al., 2006). Coronae of interlocking antigorite line the boundaries between the two domains. In magnetite-enriched rocks, the early fine-grained (<30 μm), usually euhedral magnetite (I) associated with Al-rich lizardite (Table 3) is overgrown by a new generation of coarser-grained, subhedral to anhedral disseminated magnetite (magnetite II) + euhedral antigorite + lamellar clinochlore. Clinochlore probably forms as consequence of the transformation of Al-rich lizardite to Al-poor antigorite, since its content is proportional to the amount of antigorite that replaces lizardite. The two magnetite generations have similar major element compositions (Table 3). Possible variations in trace element compositions could not be determined because of the small crystal size of magnetite I. Magnetite II can completely replace the lizardite-rich domains, but the amoeboid shape of the domains and the antigorite coronae are usually preserved (Fig. 3f, Fig. 4g, h). On the contrary, the antigorite domains and coronae show only scarce anhedral magnetite (Fig. 4g, h). A magnetite-rich diopsidite, composed of dominant fine-grained diopside (<50 μm), subordinate magnetite and minor euhedral antigorite (<150 μm; Fig. 3f; Tables 3 and 4), has been observed in contact with the magnetite-rich pegmatoid serpentinite.

4.3. Bulk rock geochemistry

Bulk rock compositions are reported in Table 4. The magnetite-poor (Fe_2O_3 <8.5 wt%) serpentinized peridotites have major and trace element concentrations typical for refractory peridotites (cf. Andreani et al., 2014; Bodinier and Godard, 2003; Niu, 2004; Paulick et al., 2006), such as low Al_2O_3 (~1-3 wt%) and TiO_2 (0.02-0.1 wt%), high Ni (~1400-2800 ppm) and Cr (~1900-2600 ppm) and low Co/Ni ratio (~0.05-0.07). The Cu and Zn contents (~20 and ~40-50 ppm, respectively) are also typical for upper mantle peridotites (cf. O'Neill and Palme, 1998; Niu 2004; Fouquet et al. 2010). The pegmatoid serpentinites have variable Al_2O_3 (~0.8-2.6 wt%), Fe_2O_3 (~4.5-10 wt%), Ni (~500-2000 ppm), and Cr (~10-2700 ppm) contents and Co/Ni ratios (~0.05-0.2). However, Cu and Zn show very little variation (~20 and ~30-40 ppm, respectively).

The magnetite-enriched (Fe_2O_3 >28 wt%) serpentinites have different compositions reflecting their distinct host rocks. The magnetite-rich pegmatoid serpentinite has a high Al_2O_3 content (~2 wt%) and a high Co/Ni ratio (~0.4), but low Ni, Cr, Cu and Zn contents (~280, ~10, ~70, ~60 ppm, respectively). The fine-grained disseminated ore has Al_2O_3, Cr and Ni contents (~1 wt%, ~2200, ~1200 ppm, respectively) in the same range as the magnetite-poor serpentinized peridotites, but has higher Cu and Zn contents (~200 and ~120 ppm, respectively) and a higher Co/Ni ratio (~0.1). With further increase in magnetite content, the concentrations of Cr (~1300 ppm) and Ni (~240 ppm) decrease, but the Co/Ni ratio increases (~0.6). The magnetite vein ore (Fe_2O_3 ~44 wt%) has low Ni (~500 ppm) and Cr (~70 ppm) contents and an intermediate Co/Ni ratio (~0.3). Moreover, it exhibits moderately high Zn (130 ppm) and the highest Cu content (~14000 ppm), which reflects the presence of chalcopyrite. The magnetite-rich diopsidite (Fe_2O_3 ~21 wt%) has a trace element composition similar to that of the pegmatoid serpentinite it is in contact with, but it has a higher Co/Ni ratio (~0.9).

In the nodular ores, the SiO_2 and MgO contents are inversely proportional to the amount of magnetite present. The Al_2O_3 and CaO concentrations are variable and reflect the different relative abundances of clinochlore and diopside (or carbonates), respectively. The TiO_2 content is generally

low (0.02 wt%), but in the ore from Site 1 it can be slightly higher (~ 0.06 wt%), consistently with the presence of Ti-rich chondrodite. The nodular ores are virtually Cr-free (~10 ppm), have low Ni (~10-110 ppm) and relatively high Co (~320-440 ppm) contents, which translate into the highest observed Co/Ni ratios (~3-30). Moreover, compared to serpentinized peridotites and pegmatoid serpentinites, they show somewhat higher Cu and Zn (~30-50 ppm and ~80-100 ppm, respectively). The nodular ores, the magnetite-rich pegmatoid serpentinite and the magnetite-rich diopsidite share significant U and Th contents, which reach the maximum values at Site 1 (U = 2.9 ppm; Th = 0.9 ppm). In both magnetite-poor and magnetite-enriched serpentinized tectonitic peridotites, U and Th contents are below the detection limits of ICP-MS analysis (<0.01 and <0.02 ppm, respectively).

The relationships between magnetite enrichment, Co/Ni ratio and Cr content are shown in Figure 5. Magnetite enrichment is generally accompanied by an increase in the Co/Ni ratio, but shows no correlation with the Cr content. In particular, the Cr content is very low (<30 ppm) in the nodular ores, in the diopsidites and in most pegmatoid serpentinites (both magnetite-poor and magnetite-enriched) and is higher (Cr >1200 ppm) in both barren and magnetite-enriched serpentinites after peridotites.

4.4. Age of the deposit

The high U (+ Th) contents in nodular ores from Site 1 and Site 3 can be attributed to the presence of uraninite inclusions in magnetite. Uraninite forms anhedral to euhedral cuboctahedral crystals, ranging in size from ~1 to 40 μm (Fig. 6a-c, e, g). Textural evidence suggests that uraninite and magnetite (+clinochlore) were contemporaneous (Fig. 6b, g). The compositions of the uraninite crystals are reported in Table 5. The U/Th ratios are variable (3 to 21), especially at Site 1, where both the highest and the lowest Th contents were measured. The FeO and CaO concentrations are relatively high (FeO = 0.8-4.9 wt%; CaO = 0.06-1.2 wt%), but they are unrelated to PbO contents,

485 which excludes late-stage alteration (Alexandre and Kyser, 2005). Excitation of the host magnetite
486 within the microprobe interaction volume could explain the presence of Fe in the analyses. On the
487 contrary, the Ca content is considered to be primary and ascribed to lattice-bound substitutions of
488 Ca for U. A less than 1 μm-thick, U-rich rim is sometimes observed in uraninite crystals (Fig. 6e),
489 and is ascribed to partial alteration.

490 The U-Th-Pb ages calculated for a group of three small (<10 μm) uraninite grains from Site 1
491 (Fig. 6a-c) are plotted in Fig. 6d. Due to the small grain size, only single-spot analyses were
492 acquired. The weighted average age is 161.8 ± 3.5 Ma (MSWD = 0.51). Figure 6f shows the ages
493 obtained for an aggregate of zoned grains from Site 1 (Fig. 6e). The crystals have a U-rich rim,
494 which testifies for partial alteration. Therefore, we only considered sixteen analyses that form a
495 plateau for PbO, UO_2 and ThO_2 concentrations (Fig. 7). The weighted average age for the plateau,
496 after rejecting two outliers, is 150.8 ± 2.0 Ma (MSWD = 1.03). The weighted average age
497 calculated for a big (~ 40 μm), unzoned uraninite crystal from Site 3 (Fig. 6g), which is intergrown
498 with magnetite and contains chlorite, is 151.9 ± 1.4 Ma (MSWD = 0.91) (Fig. 6h). Also in this case
499 only plateau PbO values were considered (Fig. 7). The two age determinations that yield the lowest
500 uncertainties and best MSWD values (i.e., close to unity) are within errors of each other and are
501 considered to be the most reliable. However, considering the limited age scatter, it is reasonable to
502 combine all the data into a single age determination, which yields a value of 152.8 ± 1.3 Ma
503 (MSWD = 1.3; Fig 6i).
504
505
506 *4.5. Geochemistry of Cogne magnetite*
507
508 The compositions of the Cogne magnetites are reported in Tables 3 and 6. The magnetites show
509 significant substitutions of Fe by Mg and Mn (Fig. 8). The concentrations of these metals are the
510 highest at Site 1 (median = ~24100 ppm and ~5000 ppm, respectively). Concentrations of Ca, Si,

Mo, Zr and Cr are generally below or close to the ICP-MS detection limits; only magnetite forming the disseminated ore from Site 2 has significant Cr contents, which can be as high as ~150 ppm. Among the other trace elements, the concentrations of Ni, Co, Ti, and Zn are generally an order of magnitude higher than those of V (Fig. 8). The highest concentrations of Co are found at Site 1 (median = ~570 ppm), whereas the lowest concentrations are in magnetite in disseminated ore from Site 2 (median = ~80 ppm). In spite of across-site variations, the Co content is fairly constant in magnetite from the same sample. The Ti content is the highest in magnetite from disseminated ore from Site 2 (median = ~570 ppm) and the lowest in magnetite from diopside-rich rocks from Site 1 and Site 3 (median = ~60 ppm). The Ni and V contents are highest in magnetite from the magnetite-rich pegmatoid serpentinite (median = ~670 ppm and ~60 ppm, respectively). The lowest Ni and V contents are observed in Site 1 ore (median = ~80 ppm) and in vein magnetite (median = ~6 ppm), although in the latter both elements are highly variable. The Zn contents show minor variability: the highest values are found in the vein magnetite (median: ~160 ppm) and the minimum values are found in magnetite from Site 3 (median: ~80 ppm).

Robust PCA indicates that the two first principal components (PC1 and PC2) can explain 97% of the variability of the magnetite compositional data and thus can adequately be used to describe the various magnetite populations. As shown by the loading plot (Fig. 9), Mg, Mn, Co and Zn are highly correlated, while Ni is anti-correlated and V and Ti vary independently from the other elements. In the PC1 vs. PC2 plot, one cluster of samples, which encompasses the magnetites in the nodular ores from Site 1 and Site 3 and the magnetite-rich diopsidite, is characterized by the highest (Mg, Mn, Co, Zn)/Ni ratios. High Ni contents are instead distinctive of disseminated magnetite in serpentinized peridotite and in the magnetite-rich pegmatoid serpentinite from Site 3 (Fig. 8). These high-Ni magnetites form two distinct groups, in which high Ni is associated with high Ti (and Cr) and high V, respectively. Vein magnetites, having a very variable Ni and low overall V, plot in an intermediate position between high-Ni and low-Ni magnetites. When plotted on the Zn vs. Co plane

(Fig. 10), most of the magnetites show a nearly constant Zn/Co ratio of ~0.28. Magnetites in the veins and in the fine-grained disseminated ore have higher Zn/Co ratios (~1).

4.6. Thermodynamic modelling

We attempted to reproduce the mineral assemblages observed at Cogne in a model seafloor hydrothermal system. The fluids produced by interaction at 400°C of modified seawater with harzburgite and Fe-gabbro (Table 2), respectively, provide two potential endmember compositions for fluids circulating in and reacting with the original oceanic substrate rocks. Harzburgite composes the uppermost part of the Cogne deposit and is the most common type of abyssal peridotite (Mével, 2003). Fe-gabbro is the most Fe-rich rock that can be found in the ophiolitic units of southern Valle d'Aosta (Benciolini et al., 1988; Bocchio et al., 2000; Dal Piaz et al., 2010; Polino et al., 2014) and it can be an efficient source of iron if altered at high temperature. Based on our calculations, dissolved Fe in the harzburgite-reacted fluid (Fig. 11a) increases from W/R ~1 to W/R ~7 where it reaches a maximum value of ~11 mmol/kg (604 ppm). The increase in Fe concentration follows the pH decrease that is in turn controlled by hydrolysis of mantle orthopyroxene, which is much more reactive than olivine at 400°C (Charlou et al. 2002). In general, the Fe-gabbro-reacted fluids are more acidic and more Fe-rich. The Fe concentration is up to one order of magnitude higher (Fig. 11b), reaching a maximum value of ~26 mmol/kg (1439 ppm) at W/R ~80. Such a high dissolved Fe content again reflects a pH minimum, which immediately follows the total breakdown of plagioclase. This is consistent with experimental evidence that plagioclase alteration to Mg-silicates (chlorite, epidote, talc) by seawater at 400°C and high W/R buffers pH to low values (Seyfried, 1987; Seyfried et al., 2010). Other major differences between the two fluid types at their Fe peak concern the concentrations of Mg and Si, which are about one order of magnitude lower and two order of magnitude higher, respectively, in the Fe-gabbro-reacted fluid. The high W/R

562 ratios required to maximize the Fe contents could potentially be achieved in a highly fractured
563 substrate, such as at the foot wall of a detachment fault in an oceanic core complex (e.g., McCaig et
564 al., 2007).

565 The harzburgite-reacted and Fe-gabbro-reacted fluids carrying the maximum dissolved Fe
566 were further reacted at either 300°C or 400°C with the different lithologies listed in Table 2. We
567 considered temperatures ≥300°C to account for the ubiquitous presence of antigorite (predominant
568 at T >300°C; Evans, 2004, 2010) in all ore assemblages at Cogne and because these high
569 temperatures disfavour substitution of Fe for Mg in minerals (especially in brucite; Klein et al.,
570 2009), thus accounting for the very high $100 \cdot Mg/(Mg+Fe)_{mol}$ ratios (Mg# >90) of gangue minerals
571 in the Cogne deposit (Table 3). Moreover, at the high temperatures considered, and especially at
572 high W/R ratios, the thermodynamic properties of the very Mg-rich gangue minerals are well
573 approximated by their Mg endmembers, hence neglecting solid solutions can be considered to be a
574 minor problem. The only mineral phase that significantly deviates from the ideal composition is
575 lizardite, which is always Al-rich (Table 3). However, textural evidence indicates that lizardite is a
576 minor relict phase that was formed during an early serpentinization event and rarely survived the
577 successive higher temperature ore-forming process (cf. section 4.1). Accounting for the presence of
578 Al-rich lizardite would not have significantly influenced the modelling of the fluid-rock system at
579 high temperature.

580 The mineral assemblages produced by hydrothermal fluid-rock interactions are shown in Figure
581 12. Magnetite is stable for both fluids over the whole considered W/R range at both 300°C and
582 400°C (with the exception of fresh troctolites reacting with harzburgite-reacted fluid at 300°C).
583 Under *rock-dominated conditions* (W/R <1), the final alteration mineral assemblages are similar for
584 both fluids: forsterite and brucite are generally formed in addition to magnetite, but their stability is
585 dependent on temperature, with forsterite being stable at higher temperature (Fig. 12b, d) than
586 brucite (Fig. 12a, c). Fayalite is predicted to form at both 300°C and 400°C in fresh troctolites and
587 pegmatoid serpentinites. The presence of pure fayalite may be an artefact induced by neglecting

588 solid solutions in olivine. Clinochlore is present in all mineral assemblages at 400°C (with the
589 exception of the model of a fresh dunite reacting with harzburgite-reacted fluid), but at 300°C it
590 forms in abundant quantities only in troctolites (both fresh and serpentinized) and pegmatoid
591 serpentinites. Diopside is abundant only in Ca-rich rocks, i.e. harzburgites and troctolites (Table 2),
592 and in troctolites it is associated with tremolite. In these rocks also minor anhydrite forms. At
593 300°C in fresh harzburgites and serpentinized dunites the diopside is soon destabilized and the
594 liberated Mg and Si combine with dissolved Al to form clinochlore. At higher temperatures this
595 reaction is limited to higher W/R ratios. Some phlogopite is produced during alteration of fresh
596 troctolites. At *intermediate W/R ratios*, diopside disappears at both 300°C and 400°C. In troctolites,
597 diopside breakdown is accompanied by an increase in the modal amount of tremolite (and fayalite
598 at 300°C). In serpentinized harzburgites, diopside reacts at 300°C with brucite and magnetite to
599 form andradite and antigorite (cf. reaction n. 44 in Frost and Beard, 2007; Fig. 12a, c). Talc
600 becomes abundant in pegmatoid serpentinites at 400°C, but at 300°C it only forms when the rocks
601 react with Fe-gabbro derived fluid. Formation of talc is enhanced by the low pH, high Si and low
602 Ca activities of the Fe-gabbro-reacted hydrothermal fluid. At *high W/R ratios*, in both fresh and
603 serpentinized dunites and harzburgites, brucite reacts with either the harzburgite-reacted fluid or the
604 Fe-gabbro reacted fluid to form antigorite or clinochlore, respectively. Talc is formed in Si-rich
605 systems, i.e. those involving Si-rich lithologies (troctolites, pegmatoid serpentinite) or fluids (Fe-
606 gabbro-reacted fluids). In the systems dominated by Fe-gabbro-reacted fluids, talc replaces
607 forsterite and antigorite, thus forming talc + magnetite + clinochlore assemblages.
608

609 ## 5. Discussion

610

611 *5.1. Cogne as an ultramafic-hosted subseafloor hydrothermal deposit*

612

613 *5.1.1. Constraints from magnetite geochemistry and ocean seafloor studies*

Important clues about the origin of the Cogne magnetite can be derived from the comparison with existing published datasets for magnetite from various genetic environments. The Cogne magnetite is poor in Ti and Cr (<640 ppm and <150 ppm, respectively), which is a typical feature for hydrothermal magnetite (Fig. 13). In fact, based on the data compiled by Dare et al. (2014), hydrothermal magnetite can be distinguished from magmatic magnetite, because the former has generally low Ti contents (<10000 ppm) and high Ni/Cr ratios (≥1), in virtue of the higher mobility of Ni in aqueous fluids. Cogne magnetite is also poor in V (<140 ppm) and rich in Mn (>2500 ppm), similar to hydrothermal magnetite from skarn deposits (Fig. 14). However, the Cogne magnetite ore was not emplaced in carbonate rocks but in mantle serpentinites, as testified by the geochemical and textural features of the host rocks.

Serpentinization of peridotites can produce magnetite that is depleted in Cr, Ti, V and Ni compared to the primary magmatic magnetite (Boutroy et al., 2014). However, serpentinization alone cannot account for the amount of magnetite observed in most of Cogne rocks. In fact, magnetite production during serpentinization is limited by the amount of FeO available in the peridotite, which is commonly less than 10 wt% (Bodinier and Godard, 2003). Therefore, an efficient mechanism of mobilization and concentration of Fe is needed to explain the formation of the Cogne deposit.

Low-T (100-300°C) hydrothermal fluids causing peridotite serpentinization at high W/R can leach Fe from the peridotite and precipitate it as magnetite in veins (up to a few cm-thick), as reported for the Bou Azzer ophiolite, Morocco (Gahlan et al., 2006). However, the compositions of Bou Azzer vein magnetites, although considerably depleted in trace elements as a consequence of their low formation temperatures (Nadoll and Koenig, 2011), are very different from those of Cogne magnetites. The latter have higher Co/Ni ratios (0.2-67 vs. 0.004-0.12) and are richer in Mn (2600-5000 vs. 400-470 ppm), Zn (80-160 vs. 3-20 ppm) and Mg (5600-24000 vs. 97-1000 ppm). These differences suggest that the formation of Cogne magnetite took place under substantially dissimilar physicochemical conditions.

Some indications on the various factors that controlled the composition of Cogne magnetite can be derived from the PCA (Fig. 9). The PC1 clearly discriminates high-(Mg, Mn, Co, Zn) magnetites in nodular ores and diopsidites from high-(Ni, V, Ti) magnetites in fine-grained disseminated ore and in magnetite-rich pegmatoid serpentinite. The relatively low Mn, Co and Zn contents in the host rocks and the fluid-compatible nature of these metals suggests that the composition of the high-(Mg, Mn, Co, Zn) magnetites was controlled by an externally-buffered fluid (cf. Dare et al., 2014; Nadoll et al., 2014). The high Co/Ni ratios these magnetites (Table 6) also support this hypothesis, because it would suggest a mafic metal source (cf. Melekestseva et al., 2013), which is in contrast with the ultramafic nature of most of the Cogne host rocks. On the contrary, the high-(Ni, V, Ti) magnetites are more enriched in elements that are weakly mobile and/or relatively abundant in the host rocks, suggesting formation under rock-buffered conditions (cf. Nadoll et al., 2014). The PC1 may thus be interpreted as reflecting magnetite formation under different W/R ratios from possibly similar parent fluids. The PC2 further discriminates between the different host rocks (i.e. high-V magnetite in pegmatoid serpentinite and high-Ti magnetite in serpentinized tectonitic peridotites). Magnetite in veins shows intermediate geochemical features between hydrothermal fluid-buffered and host rock-affected compositions.

Hydrothermal fluids carrying a significant load of transition metals (high Fe, Mn, Cu, Zn ± Co ± Ni) issue from ultramafic substrates in high-T (>350°C) hydrothermal systems associated with oceanic core complexes in slow-spreading mid-oceanic ridges, such as at Rainbow and Logatchev on the Mid-Atlantic Ridge (Douville et al. 2002; Andreani et al., 2014). In particular, the hydrothermal vent fluids at Rainbow are the richest in Co (Douville et al., 2002), have the highest Co/Ni ratios (~4) and are probably saturated in magnetite + chlorite + talc (Seyfried et al., 2011). The surveyed portion of the Rainbow hydrothermal deposit is almost entirely made up of sulphides (Fouquet et al., 2010; Marques et al., 2006, 2007), as expected for the upper part of a seafloor hydrothermal system, where the hot hydrothermal fluid mixes with seawater (Janecky and Seyfried, 1984). Notwithstanding this, at Rainbow, hydrothermal magnetite is locally abundant in

666 serpentinites hosting sulphide stockworks and in semi-massive sulphides, where magnetite
667 sometimes replaces pyrite (Marques, 2005). Magnetite forming coarse-grained disseminations in
668 the serpentinites that host stockworks at Rainbow precipitated later than the sulphides during a
669 distinct hydrothermal stage (Marques et al., 2006) and, notably, has a similar geochemical
670 fingerprint as magnetite in fine-grained disseminations in serpentinized peridotites at Cogne (the
671 concentrations of the trace elements, with the exception of Si, are in the same order of magnitude).
672 Recently, Yıldırım et al. (2016) described a hydrothermal magnetite mineralization in a non-
673 metamorphic volcanogenic massive-sulphide (VMS) deposit from the Upper Triassic-Upper
674 Cretaceous Koçali complex, a Tethyan ophiolite in Turkey. These findings and the above
675 observations support the possibility that Cogne magnetite has directly formed in a seafloor
676 hydrothermal system. The presence of a positive magnetic anomaly at Rainbow has been ascribed
677 to a ~$2 \cdot 10^6$ m^3 magnetite-rich stockwork zone (Szitkar et al., 2014). If this volume was entirely
678 composed of magnetite, it would correspond to 10 Mt of mineral, which is on the same order of
679 magnitude as the estimated amount of magnetite at Cogne (~12 Mt). It is worth noting that the
680 Rainbow hydrothermal system is still highly active (Fouquet et al. 2010) and its vent fluids are
681 magnetite-saturated (Seyfried et al., 2011). It can thus be inferred that the Rainbow hydrothermal
682 system may eventually produce at depth a magnetite deposit of comparable size as Cogne.

683 In such a scenario, the general scarcity of sulphides at Cogne, along with their presence in
684 the veins above the main magnetite bodies, suggest that the exposed mineralized section represents
685 the deep segment of a seafloor, ultramafic-hosted, high-temperature hydrothermal system, which
686 was possibly associated with shallower, now eroded, sulphide-rich bodies. According to this
687 interpretation, the magnetite + sulphide veins and fine-grained disseminations in the hanging wall
688 serpentinite (Site 2) may mark the transition between the magnetite-rich and the sulphide-rich
689 portions of the hydrothermal system (Fig. 15).

690

691 *5.1.2. Geological, geochronological and textural constraints*

692 The Cogne mantle peridotites underwent complete serpentinization at 200-300°C beneath the
693 seafloor of the Jurassic Piedmont-Liguria ocean (Carbonin et al., 2014). Our radiometric data on
694 magnetite-associated uraninite (152.8 ± 1.3 Ma) places the ore-forming event in proximity of the
695 Kimmeridgian-Tithonian boundary (152.1 ± 0.9 Ma). This age overlaps with that of the spreading
696 of the Piedmont-Liguria ocean, as inferred by biochronological dating of supra-ophiolitic deep-sea
697 sediments (radiolarites), whose oldest ages span from Late Bajocian to Middle Bathonian (~ 168
698 Ma; Cordey et al., 2012), and by radiometric dating of magmatic rocks, which places the latest
699 magma pulses (mainly plagiogranites) in the Western Alps and Liguria in the Kimmeridgian-
700 Tithonian (~157.3 ± 1.0 - ~145.5 Ma; Lombardo et al., 2002; Manatschal and Müntener, 2009 and
701 references therein).

702 Very little information can be obtained about the original lithological and thermal structure
703 of the oceanic lithosphere at Cogne, because of the limited exposure. Some indirect information can
704 be obtained from the nearby Mt. Avic serpentinite massif (Fig. 1). Although located in a different
705 structural position in the orogen (see Dal Piaz et al., 2010), the Mt. Avic massif provides the most
706 complete section of the oceanic lithosphere of the Alpine Tethys in the southern Valle d'Aosta
707 region. In the Mt. Avic massif, dominant serpentinized mantle peridotites, associated with gabbroic
708 intrusions (Mg-metagabbros), rodingitic dykes, minor Fe-Ti-oxide metagabbros and other
709 metabasites (Dal Piaz et al., 2010; Fontana et al. 2008, 2015; Panseri et., al 2008), are thought to
710 have been exposed on the seafloor in an oceanic core complex (Tartarotti et al., 2015). This is
711 consistent with the proposed slow- to ultra-slow nature of the Piedmont-Liguria ocean (Manatschal
712 et al., 2011; Manatschal and Müntener, 2009; Piccardo et al., 2008). Jurassic magmatic activity in
713 the Mt. Avic massif was sufficient to sustain high-temperature hydrothermal convection cells, as
714 testified by widespread, small, massive sulphide (Cu-Fe-Zn) deposits, which are mostly associated
715 with metabasites (Castello et al., 1980; Castello, 1981; Martin et al., 2008; Dal Piaz et al., 2010;
716 Fantone et al., 2014) and are thought to have formed in the seafloor (Martin et al., 2008). The
717 distinctive enrichment in Co and Cu observed in Cogne nodular and vein magnetite ores,

718 respectively, as well as the low Ni content in all magnetite ore types, suggests a contribution from
719 mafic sources or a combined contribution from ultramafic and mafic sources, as observed in some
720 ultramafic-hosted, mid-ocean ridge, hydrothermal deposits (e.g. Rainbow, Fouquet el al., 2010;
721 Marques et al., 2006; Semenov, Melekestseva et al., 2014) and in other ultramafic-hosted VMS
722 deposits in ophiolitic belts (Melekestseva et al., 2013). In analogy with these modern and ancient
723 examples, also at Cogne the presence of deep magmatic intrusions (gabbro) would be required to
724 provide heat and suitable chemical conditions (low pH) to produce metal-rich fluids (e.g., Marques
725 et al., 2006; Seyfried et al., 2011). Gabbroic intrusions, mainly represented by gabbros and Fe-Ti
726 gabbros, are not observed in the small Cogne unit, but are common in the wider Mt. Avic area (see
727 above) and in the other ophiolitic units in southern Valle d'Aosta (Grivola-Urtier and Zermatt-Saas
728 units; Benciolini et al., 1988; Bocchio et al., 2000; Dal Piaz et al., 2010; Polino et al., 2014).
729 Therefore, we infer that similar rock types could have occurred also at Cogne in the original oceanic
730 lithosphere section.

731 The texture, geochemistry (low Co/Ni, high Cr) and relict mineralogy (bastites, Mg-Al-rich
732 chromite) of Site 2 magnetite-enriched serpentinites suggest that the host rock was a harzburgitic
733 mantle tectonite, with composition comparable with that of modern abyssal peridotites. However,
734 chemical and textural evidence from both Site 1 and Site 3 indicates that part of the hydrothermal
735 ore was emplaced in more atypical serpentinites, which exhibit a ghost pegmatoid texture marked
736 by interlobate domains separated by coronae structures (Fig. 3f). Similar textures have been
737 described in some troctolites from modern oceanic and ancient ophiolitic settings (Blackman et al.,
738 2006; Renna and Tribuzio, 2011). These rocks are interpreted to have formed from melt-
739 impregnation and melt-peridotite reactions, which dissolved orthopyroxene and partially dissolved
740 olivine producing rounded or embayed grain boundaries (Drouin et al., 2009; Renna and Tribuzio,
741 2011; Suhr et al., 2008). In particular, olivine-rich troctolites originating from melt-peridotite
742 reactions are usually coarse-grained and can show a harrisitic texture (Renna and Tribuzio, 2011),
743 which is reminiscent of the "harrisitic" texture of some nodular ores at Cogne. This suggests that

744 many, if not most, nodular ores at Cogne formed by hydrothermal alteration of original
745 serpentinized troctolites, with magnetite preferentially replacing the original olivine domains.
746
747 *5.1.3. Insights from thermodynamic modelling*
748 From a qualitative point of view, interaction of various types of fresh or serpentinized mantle rocks
749 with either a harzburgite-reacted fluid at intermediate to high W/R or a Fe-gabbro-reacted
750 hydrothermal fluid at intermediate W/R (Fig. 12) can produce mineral assemblages made of
751 magnetite + antigorite + clinochlore ± brucite (at 300°C) ± forsterite (at 400°C), which resemble the
752 most common mineral assemblages in the Cogne magnetite ores. However, even when the natural
753 mineral assemblage is qualitatively reproduced, the calculated modal magnetite content invariably
754 remains too low to produce a magnetite ore. This indicates that our model fluids are not sufficiently
755 Fe-rich to account for the formation of the Cogne deposit. Note that a Rainbow-type fluid (Table 7)
756 would produce broadly similar mineral assemblages as our model fluids, since its Na, Mg, Si, Fe, Cl
757 concentrations are fairly similar. We could not envisage any other reasonable substrate lithology
758 which could have released significantly higher Fe to the hydrothermal fluids under reasonable
759 conditions. This suggests that additional processes other than simple seawater/rock reactions have
760 played a role in the formation of the magnetite parent fluids.
761 One such process could be phase separation in the hydrothermal fluid, which could have
762 produced brines enriched in weakly volatile Fe. Phase separation is commonly invoked to explain
763 the wide chlorinity range observed in modern seafloor hydrothermal vent fluids (e.g., Bischoff and
764 Rosenbauer, 1987; Charlou et al., 2002; Douville et al., 2002; Foustoukos and Seyfried, 2007;
765 Pester et al., 2014; Seyfried et al., 2011). A higher chlorinity would enhance solubility of metals as
766 chloride complexes. At the same time, H_2S partitioning into the vapour phase would cause sulphide
767 undersaturation in the brine (Bischoff and Rosenbauer, 1987; Fouquet et al., 2010; Seyfried et al.,
768 2004; Seyfried at al., 2010; Von Damm, 2004), thus delaying sulphide precipitation. This is in
769 agreement with the general scarcity of sulphides in the Cogne magnetite ores. The presence of

chalcophile metals in the fluid is still testified by Cu sulphides in magnetite veins from Site 2. In this case, the transition from bornite + magnetite to chalcopyrite + magnetite assemblages suggests a progressive variation in the parent fluids towards higher H_2S activity or lower Cu/Fe ratios (cf. Seyfried et al., 2004, 2010).

Another process which could potentially lead to enhanced Fe concentrations in the fluid is the incorporation of a magmatic gaseous component, which could promote acidification and thus increase Fe solubility (cf. Berkenbosch et al., 2012; de Ronde et al., 2011). However, assuming a gas composition similar to that of gases emitted from mafic lavas (Erta 'Ale volcano, Ethiopia; Sawyer et al., 2008), it can be calculated that a relatively high condensed gas/fluid mass ratio of 1:10 would increase the Fe concentrations only by a factor of ~2.3. This increase is too small to allow a significant increase in the final amount of precipitated magnetite. Therefore, phase separation remains the most likely hypothesis.

Another feature that is not explained by our models is the diopside-rich gangue observed at Site 3. Textural relationships suggest that diopside formed during a late stage of magnetite mineralization, most likely from a fluid with higher pH and/or higher Ca^{2+} activity (see Fig. 9 in Bach and Klein, 2009). This fluid could have derived from serpentinization of country peridotites and troctolites, and may thus have some affinity with rodingite-forming fluids. Alternatively, a higher Ca content could result from more extensive interaction with gabbroic rocks. The possible role of gabbroic rocks in producing Ca-Si-(Al)-rich fluids has been suggested, for instance, for fluids responsible for strong calcic metasomatism in fault zones in modern oceanic core complexes (Boschi et al., 2006).

5.2. Alternative hypotheses

As ultramafic rocks in ophiolitic massifs often contain accumulations of chromite (e.g., Bédard and Hébert, 1998), a potential origin of magnetite in Sites 1 and 3 could be by leaching of Cr from former chromitite bodies. Indeed, Cr appears to be mobile during high-temperature (>500-550°C) peridotite-water interactions, as shown by Arai and Akizawa (2014) for the Oman ophiolite. Also, in the Mt. Avic massif, some small-scale magnetite ores were apparently formed after former chromitites (Diella et al., 1994; Rossetti et al., 2009). There are two lines of evidence against this hypothesis for the Cogne magnetite. First, in the Mt. Avic ores, chromite is still preserved in the cores of the magnetite grains (Diella et al., 1994; Fontana et al., 2008; Rossetti et al., 2009), whereas neither chromite relicts nor Cr-rich magnetite cores are found in nodular and vein ores at Cogne. Second, there is no evidence for a high-temperature alteration at Cogne such as that described in the Oman ophiolite by Arai and Akizawa (2014). At the temperatures under which serpentinization and successive hydrothermal metasomatism at Cogne took place (200-300°C and 300°-400°C, respectively; Carbonin et al., 2014), Cr is essentially immobile and any Cr dissolved at higher temperatures deeper in the system should be precipitated (Arai and Akizawa, 2014). The immobility of Cr during magnetite mineralization is testified by the mantle tectonites containing the fine-grained disseminated magnetite from Site 2, which have similar bulk-rock Cr content as their magnetite-poor counterparts (Fig 5). In these rocks, the original Mg-Al-rich chromite (the main Cr carrier) was replaced *with no Cr loss* by Fe-rich chromite + Cr-rich chlorite, according to reactions of the type

$$24\ (Mg,Fe)(Al,Cr)_2O_4 + 18\ (Mg,Fe,Al)_3Si_2O_5(OH)_4 + 12H_2O + O_2 \rightarrow$$

Mg-Al-rich chromite serpentine

$$12(Mg,Fe,Al,Cr)_5(Si_3Al)O_{10}(OH)_8 + 14\ (Mg,Fe)(Cr,Fe,Al)_2O_4$$

Cr-rich chlorite Fe-rich chromite

(cf. Mellini et al., 2005; Merlini et al., 2009), and then overgrown by Cr-poor magnetite (Fig. 4d). The P-T conditions for the subsequent Alpine metamorphism at Cogne are not precisely known. However, assuming a typical subduction geothermal gradient (<10°C/km), the coexistence of

821 lizardite and antigorite in both serpentinized peridotites and pegmatoid serpentinites suggests
822 temperatures not exceeding 390°C (Schwartz et al., 2013), which are too low to determine
823 significant mobilization of Cr.

824 Iron (Mn) oxyhydroxides and Fe sulphide deposits are the most common forms of Fe
825 accumulation in modern seafloor hydrothermal settings (e.g., Rona, 1988). In principle, magnetite
826 may form by reduction and dehydration of Fe-oxyhydroxides or by desulphurization of Fe-
827 sulphides during metamorphism. However, our geochronological data demonstrate that the
828 magnetite-forming event was coeval with the spreading of the Piedmont-Liguria ocean and thus
829 predates Alpine metamorphism. Also the geochemistry of Cogne magnetite ores and associated
830 rocks contradicts the metamorphic hypothesis. In fact, in Fe-oxyhydroxide accumulations, an
831 enrichment in trace elements such as P and Sr is typically observed (e.g., Hekinian et al., 1993;
832 Puteanus et al., 1991). A similar enrichment is indeed preserved in seafloor hydrothermal Mn-(Fe)
833 deposits in southern Valle d'Aosta ophiolites (median P_2O_5 = 0.06 wt%, median Sr = 1650 ppm;
834 Tumiati et al., 2010), which were metamorphosed up to eclogite-facies conditions (T = 550 ± 60°C,
835 P = 2.1 ± 0.3 GPa; Martin et al., 2008; Tumiati et al., 2015), but it is not observed in Cogne ores
836 (P_2O_5 ≤0.01 wt%, median Sr = 1.6 ppm). In the same ophiolites, sulphide (pyrite + chalcopyrite)
837 deposits show no evidence of S mobilization and depletion linked to subduction metamorphism
838 (Giacometti et al., 2014). Consistently, serpentinized mantle tectonites overlying the Cogne
839 magnetite orebody are not depleted in S (Table 4).
840
841 *5.3. The role of the Alpine event*
842
843 The present structural position of the Cogne serpentinite, the lithological associations and the shape
844 of the orebodies are in part the result of the tectonic activity that accompanied the Alpine
845 orogenesis. The main magnetite orebodies at Site 1 and Site 3 behaved as rigid masses during the
846 early ductile deformation events and they were affected by only low degrees of shear deformation,

847 thus preserving the original textures and the proportions between magnetite and gangue minerals.
848 The Alpine deformation was more intense at Site 2, which was probably located in a peripheral
849 position with respect to the main orebody, where the fine-grained disseminated ores and the
850 associated veins were dismembered into lenses. The Alpine metamorphism did not promote
851 significant magnetite remobilization, as testified by the lack of isotopic resetting in uraninite
852 inclusions in magnetite. The Alpine metamorphism is possibly responsible for the transformation of
853 lizardite into antigorite, which is observed also in rocks that do not contain hydrothermal
854 mineralization (i.e. magnetite-poor serpentinized peridotites and pegmatoid serpentinites). In any
855 case the metamorphic temperatures were not sufficient to cause significant serpentine dehydration,
856 since neoblastic forsterite is not widespread and is only found within the nodular ore at Site 1. The
857 restriction of neoblastic forsterite to this specific site suggests that its formation could be related to
858 higher temperature conditions (~400°C) being attained locally during the magnetite hydrothermal
859 event, rather than to the subsequent metamorphism. Based on the above considerations, we
860 conclude that Alpine metamorphism did not play a significant role in concentrating magnetite,
861 although Alpine deformation may have pulled away portions of the deposit (now exposed at sites 1,
862 2 and 3) that could have been much closer to one another in their original oceanic setting.
863
864 *5.4 Stages of formation of the Cogne deposit*
865
866 Considering all available data, we propose the following sequence of events for the formation of the
867 Cogne deposit (Fig. 15):
868 1) Formation of an oceanic core complex made of tectonitic peridotites, containing bodies of
869 gabbros and Cr-poor melt-impregnated peridotites (troctolites).
870 2) Extensive low-temperature serpentinization, producing lizardite serpentinites containing a first
871 generation of disseminated magnetite (Cr-bearing in mantle tectonites and Cr-free in melt

872 impregnated peridotites). This process probably occurred at high water/rock ratios and determined
873 the complete serpentinization of the primary silicates and an extensive loss of Ca.
874 3) Production of a high-temperature, Fe-rich hydrothermal fluid by reaction of downwelling
875 seawater with substrate rocks. The involvement of Fe-gabbros in the reaction zone is likely, as this
876 would enhance the content of Fe in the fluid.
877 4) Phase separation in the upwelling hydrothermal fluid, producing a more Fe-rich brine.
878 5) Reaction of the upwelling hot brine (~300–400°C) with various lithologies (serpentinites after
879 mantle tectonites and troctolites) at various fluid/rock ratios, producing the dissolution of lizardite
880 and the precipitation of abundant magnetite along with antigorite and clinochlore (± brucite and
881 forsterite), forming fine-grained disseminated, nodular and massive replacive ores. Further
882 upwelling of the magnetite-buffered fluid produced magnetite + Cu-sulphide + antigorite veins and
883 fine-grained disseminations in shallower serpentinites.
884 6) Circulation of late fluids with higher pH and/or higher Ca^{2+} activity, producing diopside-rich,
885 magnetite-bearing metasomatic rocks.
886

887 ## 6. Conclusions

888

889 The Cogne magnetite deposit was formed at ~150 Ma by hydrothermal processes during an
890 advanced stage of the opening of the Piedmont–Liguria ocean. Based on geological and
891 petrographic features and on geochemical and mineralogical similarities with some modern
892 ultramafic-hosted VMS deposits on mid-ocean ridges, the exposed mineralized section at Cogne
893 may represent the deep segment of a seafloor, high-temperature (~300–400°C) hydrothermal
894 system, which was possibly associated with shallower, now eroded, sulphide-rich bodies (Fig. 15).
895 As suggested by thermodynamic modelling, simple seawater-rock interactions cannot produce the
896 Fe endowment observed at Cogne. Fractionation processes such as phase separation were probably
897 critical to generate sufficiently Fe-rich hydrothermal fluids capable to precipitate large amounts of

magnetite in various types of mantle host-rocks. The possible occurrence of similar ultramafic-hosted magnetite deposits in present-day oceanic settings could contribute to explain the presence of significant magnetic anomalies centred on active and inactive ultramafic-hosted hydrothermal fields (Fujii et al., 2016; Szitkar et al., 2014; Tivey and Dyment, 2010).

Acknowledgements

We thank Raul Carampin (CNR, IGG, Padua) and Andrea Risplendente (Earth Sciences Department, University of Milan) for the technical assistance with the electron microprobe analyses. We are also grateful to Drs. Andreas Klügel and Patrick Monien ("Petrology of the Ocean Crust" research group, University of Bremen, Germany) for providing scientific and technical support during LA-ICP-MS measurements. We thank "Assessorato Territorio e Ambiente" of the Valle d'Aosta region for providing access to the archives of the Cogne mine. We are grateful to Patrick Nadoll and Paola Tartarotti for their constructive reviews and suggestions. This work was carried out during LT's PhD at the University of Padua. PN acknowledges financial support by Progetto di Ateneo 2013 CPDA138741 "Copper metallogenesis and provenancing in the Alpine realm" (University of Padua).

References

Alexandre P and Kyser TK (2005) Effects of cationic substitutions and alteration in uraninite, and implications for the dating of uranium deposits. Can Mineral 43:1005–1017

923 Andreani M, Escartin J, Delacour A, Ildefonse B, Godard M, Dyment J, Fallick AE, Fouquet Y
924 (2014) Tectonic structure, lithology, and hydrothermal signature of the Rainbow massif
925 (Mid-Atlantic Ridge 36° 14′ N). Geochem Geophy Geosy 15:3543–3571
926
927 Arai S, Akizawa N (2014) Precipitation and dissolution of chromite by hydrothermal solutions in
928 the Oman ophiolite: New behavior of Cr and chromite. Am Mineral 99:28–34
929
930 Bach W, Klein F (2009) The petrology of seafloor rodingites: insights from geochemical reaction
931 path modeling. Lithos, 112:103–117
932
933 Bédard JH, Hébert R (1998) Formation of chromitites by assimilation of crustal pyroxenites and
934 gabbros into peridotitic intrusions: North Arm Mountain massif, Bay of Islands ophiolite,
935 Newfoundland, Canada. J Geophys Res-Sol Ea 103:5165–5184
936
937 Benciolini L, Lombardo B, Martin S (1988) Mineral chemistry and Fe/Mg exchange
938 geothermometry of ferrogabbro-derived eclogites from the Northwestern Alps. Neues Jb Miner Abh
939 159:199–222
940
941 Berkenbosch HA, de Ronde CEJ, Gemmel JB, McNeil AW, Goemann K (2012) Mineralogy and
942 formation of black smoker chimneys from Brothers submarine volcano, Kermadec Arc. Econ Geol
943 107:1613–1633
944
945 Berndt ME, Seyfried WE, Janecky DR (1989) Plagioclase and epidote buffering of cation ratios in
946 mid-ocean ridge hydrothermal fluids: experimental results in and near the supercritical region.
947 Geochim Cosmochim Ac 53:2283–2300
948

949 Bischoff JL, Rosenbauer RJ (1987) Phase separation in seafloor geothermal systems; an
950 experimental study of the effects on metal transport. Am J Sci 287:953–978
951
952 Blackman DK, Ildefonse B, John BE, Ohara Y, Miller DJ, MacLeod CJ and Expedition 304/305
953 Scientists (2006) Proceedings of the Integrated Ocean Drilling Program, Volume 304/305, College
954 Station, Texas, Integrated Ocean Drilling Program Management International, Inc.
955
956 Bocchio R, Benciolini L, Martin S, Tartarotti P (2000) Geochemistry of eclogitised Fe-Ti gabbros
957 from various lithological settings (Aosta Valley ophiolites, Italian western Alps). Protolith
958 composition and eclogitic paragenesis. Period Mineral 69:217–237
959
960 Bodinier J-L and Godard M (2003) Orogenic, ophiolitic, and abyssal peridotites. In: Turekian KK
961 and Holland HD (eds) The Mantle and Core: Treatise on Geochemistry, 2nd edn. Elsevier, Oxford,
962 pp 103-167
963
964 Boschi C, Früh-Green GL, Delacour A, Karson JA, Kelley DS (2006) Mass transfer and fluid flow
965 during detachment faulting and development of an oceanic core complex, Atlantis Massif (MAR
966 30°N). Geochem Geophy Geosys 7
967
968 Boutroy E, Dare SA, Beaudoin G, Barnes SJ, Lightfoot PC (2014) Magnetite composition in Ni-
969 Cu-PGE deposits worldwide: application to mineral exploration. J Geochem Explor 145:64–81
970
971 Bowles JFW (1990). Age dating of individual grains of uraninite in rocks from electron microprobe
972 analyses. Chem Geol 83:47–53
973

974 Bowles JF (2015) Age Dating from Electron Microprobe Analyses of U, Th, and Pb: Geological
975 Advantages and Analytical Difficulties. Microsc Microanal 21:1114–1122
976
977 Caby R (1981) Le Mésozoïque de la zone du Combin en Val d'Aoste (Alpes Graies): imbrications
978 tectoniques entre séries issues des domaines pennique, austroalpin et océanique. Géologie Alpine
979 57:5–13
980
981 Carbonin S, Martin S, Tumiati S, Rossetti P (2014) Magnetite from the Cogne serpentinites
982 (Piemonte ophiolite nappe, Italy). Insights into seafloor fluid–rock interaction. Eur J Mineral 27:31–
983 50
984
985 Caruso LJ, Chernosky JV (1979) The stability of lizardite. Can Mineral 17:757–769
986
987 Castello P, Dal Piaz GV, Gosso G, Kienast JR, Martin S, Natale P, Nervo R, Polino R, Venturelli G
988 (1980) The Piedmont ophiolite nappe in the Aosta Valley and related ore deposits. In: Gruppo di
989 Lavoro sulle Ofioliti Mediterranee. VI ophiolite field conference, Firenze. Field excursion book, pp.
990 171–192
991
992 Castello P (1981) Inventario delle mineralizzazioni a magnetite, ferro-rame e manganese del
993 complesso piemontese dei calcescisti con pietre verdi in Valle d'Aosta. Ofioliti 6:5–46
994
995 Charlou JL, Donval JP, Fouquet Y, Jean-Baptiste P, Holm N (2002) Geochemistry of high H_2 and
996 CH_4 vent fluids issuing from ultramafic rocks at the Rainbow hydrothermal field (36°14′N, MAR).
997 Chem Geol 191:345–359
998

Cocherie A and Albarede F (2001) An improved U-Th-Pb age calculation for electron microprobe dating of monazite. Geochim Cosmochim Ac 65:4509–4522

Cocherie A and Legendre O (2007) Potential minerals for determining U–Th–Pb chemical age using electron microprobe. Lithos 93:288–309

Compagnoni R, Elter G, Fiora L, Natale P, Zucchetti S (1979) Nuove osservazioni sul giacimento di magnetite di Cogne in Valle d'Aosta. Rend Soc Min Petr 35:755–766

Compagnoni R, Elter G, Fiora L, Natale P, Zucchetti S (1981) Magnetite deposits in serpentinized lherzolites from the ophiolitic belt of the Western Alps, with special reference to the Cogne deposit (Aosta Valley). In: Proceedings of the Intern. Symp. Mafic and Ultramafic Complexes, Athens, pp 376–394

Cordey F, Tricart P, Guillot S, Schwartz S (2012) Dating the Tethyan Ocean in the Western Alps with radiolarite pebbles from synorogenic Oligocene molasse basins (southeast France). Swiss J Geosci 105:39–48

Cortiana G, Dal Piaz GV, Del Moro A, Hunziker JC, Martin S (1998) 40Ar-39Ar and Rb-Sr dating of the Pillonet klippe and Sesia-Lanzo basal slice in the Ayas valley and evolution of the Austroalpine-Piedmont nappe stack. Memorie di Scienze Geologiche 50:177–194

Cross A, Jaireth S, Rapp R, Armstrong R (2011). Reconnaissance-style EPMA chemical U–Th–Pb dating of uraninite. Austr J Earth Sci 58:675–683

1024 Dal Piaz G, Cortiana G, Del Moro A, Martin S, Pennacchioni G, Tartarotti P (2001) Tertiary age
1025 and paleostructural inferences of the eclogitic imprint in the Austroalpine outliers and Zermatt–Saas
1026 ophiolite, western Alps. Int J Earth Sci 90:668–684
1027
1028 Dal Piaz GV, Bistacchi A, Massironi M (2003) Geological outline of the Alps. Episodes 26:175-
1029 180
1030
1031 Dal Piaz GV, Gianotti F, Monopoli B, Pennacchioni G, Tartarotti P, Schiavo A (2010) Note
1032 illustrative della carta geologica d'Italia alla scala 1:50.000 Chatillon F. 91. Ispra-Servizio
1033 Geologico d'Italia, Treviso
1034
1035 Dare SA, Barnes SJ, Beaudoin G, Méric J, Boutroy E, Potvin-Doucet C (2014) Trace elements in
1036 magnetite as petrogenetic indicators. Miner Deposita 49:785–796
1037
1038 Debret B, Andreani M, Muñoz M, Bolfan-Casanova N, Carlut J, Nicollet C, Schwartz S, Trcera N
1039 (2014) Evolution of Fe redox state in serpentine during subduction. Earth Planet Sci Lett 400:206–
1040 218
1041
1042 De Giusti F, Dal Piaz GV, Massironi M, Schiavo A (2003) Carta geotettonica della Valle d'Aosta.
1043 Mem Sci Geol 55:129–49
1044
1045 De Graciansky PC, Roberts D, Tricart P (2011) The Western Alps from rift to passive margin to
1046 orogenic belt: An integrated geosciences overview. Elsevier, Amsterdam
1047

Della Giusta A, Carbonin S, Russo U (2011) Chromite to magnetite transformation: compositional variations and cation distributions (southern Aosta Valley, Western Alps, Italy). Period Mineral 80:1–17

de Ronde CEJ, Massoth GJ, Butterfield DA, Christenson BW, Ishibashi J, Ditchburn RG, Hannington MD, Brathwaite RL, Lupton JE, Kamenetsky VS, Graham IJ, Zellmer GF, Dziak RP, Embley RW, Dekov VM, Munnik F, Lahr J, Evans LJ, Takai K (2011) Submarine hydrothermal activity and gold-rich mineralization at Brothers Volcano, Kermadec Arc, New Zealand. Miner Deposita 46:541–584

Di Colbertaldo D, Di Furia E, Rossi F (1967) Il giacimento a magnetite di Cogne in Val d'Aosta. Istituto Lombardo, A101:361–394

Diella V, Ferrario A, Rossetti P (1994) The magnetite ore deposits of the southern Aosta Valley: chromitite transformed during an Alpine metamorphic event. Ofioliti 19:247–256

Ding K, Seyfried WE (1992) Determination of Fe-Cl complexing in the low pressure supercritical region (NaCl fluid): Iron solubility constraints on pH of subseafloor hydrothermal fluids. Geochim Cosmochim Ac 56:3681–3692

Douville E, Charlou JL, Oelkers EH, Bienvenu P, Colon CJ, Donval JP, Fouquet Y, Prieur D, Appriou P (2002) The rainbow vent fluids (36 14′ N, MAR): the influence of ultramafic rocks and phase separation on trace metal content in Mid-Atlantic Ridge hydrothermal fluids. Chem Geol 184:37–48

1074 Drouin M, Godard M, Ildefonse B, Bruguier O, Garrido CJ (2009) Geochemical and petrographic
1075 evidence for magmatic impregnation in the oceanic lithosphere at Atlantis Massif, Mid-Atlantic
1076 Ridge (IODP Hole U1309D, 30 N). Chem Geol 264:71–88.
1077
1078 Dupuis C, Beaudoin G (2011) Discriminant diagrams for iron oxide trace element fingerprinting of
1079 mineral deposit types. Miner Deposita 46:319–335
1080
1081 Edmonds H (2010) Chemical signatures from hydrothermal venting on slow spreading ridges. In:
1082 Rona PA, Devey CW, Dyment J, Murton BJ (eds) Diversity of hydrothermal systems on slow
1083 spreading ocean ridges, American Geophysical Union, Washington, DC, pp. 27–42
1084
1085 Evans BW (2004) The serpentinite multisystem revisited: chrysotile is metastable. Int Geol Rev
1086 46:479–506
1087
1088 Evans BW (2010) Lizardite versus antigorite serpentinite: magnetite, hydrogen, and life (?).
1089 Geology 38:879–882
1090
1091 Fantone I, Grieco G, Strini A, Cavallo A (2014) The effect of Alpine metamorphism on an oceanic
1092 Cu-Fe sulfide ore: the Herin deposit, Western Alps, Italy. Period Mineral 83:345–365
1093
1094 Filzmoser P, Hron K, Reimann C (2009) Principal component analysis for compositional data with
1095 outliers. Environmetrics 20:621–632
1096
1097 Filzmoser P, Hron K (2011) Robust statistical analysis. In: Pawlowsky-Glahn V, Buccianti A (eds)
1098 Compositional data analysis. Theory and applications. John Wiley & Sons, Chichester (UK), pp.
1099 59-72

Fontana E, Panseri M, Tartarotti P (2008) Oceanic relict textures in the Mount Avic serpentinites, Western Alps. Ofioliti 33:105–118

Fontana E, Tartarotti P, Panseri M, Buscemi S (2015) Geological map of the Mount Avic massif (Western Alps Ophiolites). Journal of Maps 11:126–135

Fouquet Y, Cambon P, Etoubleau J, Charlou JL, Ondréas H, Barriga FJAS, Cherkashov G, Semkova T, Poroshina I, Bohn M, Donval JP, Henry K, Murphy P, Rouxel1 O (2010) Geodiversity of hydrothermal processes along the Mid-Atlantic Ridge and ultramafic-hosted mineralization: a new type of oceanic Cu-Zn-Co-Au volcanogenic massive sulfide deposit. In: Rona PA, Devey CW, Dyment J, Murton BJ (eds) Diversity of hydrothermal systems on slow spreading ocean ridges, American Geophysical Union, Washington, DC, pp. 321–367

Foustoukos DI, Seyfried WE (2007) Fluid phase separation processes in submarine hydrothermal systems. Rev Mineral Geochem 65:213–239

Frost BR, Beard JS (2007) On silica activity and serpentinization. J Petrol 48:1351–1368

Fujii M, Okino K, Sato T, Sato H, Nakamura K (2016) Origin of magnetic highs at ultramafic hosted hydrothermal systems: Insights from the Yokoniwa site of Central Indian Ridge. Earth Planet Sci Lett 441:26–37

Gahlan HA, Arai S, Ahmed AH, Ishida Y, Abdel-Aziz YM, Rahimi A (2006) Origin of magnetite veins in serpentinite from the Late Proterozoic Bou-Azzer ophiolite, Anti-Atlas, Morocco: An implication for mobility of iron during serpentinization. J Afr Earth Sci 46: 318–330

Giacometti F, Evans KA, Rebay G, Cliff J, Tomkins AG, Rossetti P, Vaggelli G, Adams DT (2014) Sulfur isotope evolution in sulfide ores from Western Alps: Assessing the influence of subduction-related metamorphism. Geochem Geophys Geosys 15:3808–3829

Govindaraju K (1994) compilation of working values and sample description for 383 geostandards. Geostandard Newslett 18:1–158

Groppo C, Rinaudo C, Cairo S, Gastaldi D, Compagnoni R (2006) Micro-Raman spectroscopy for a quick and reliable identification of serpentine minerals from ultramafics. Eur J of Mineral 18:319–329

Hekinian R, Hoffert M, Larque P, Cheminee JL, Stoffers P, Bideau D (1993) Hydrothermal Fe and Si oxyhydroxide deposits from South Pacific intraplate volcanoes and East Pacific Rise axial and off-axial regions. Econ Geol 88:2099–2121

Hiess J, Condon DJ, McLean N, Noble SR (2012) 238U/235U systematics in terrestrial uranium-bearing minerals. Science 335:1610–1614

Ho PC, Palmer DA, Mesmer RE (1994) Electrical conductivity measurements of aqueous sodium chloride solutions to 600 C and 300 MPa. J Solution Chem 23:997–1018

Ho PC, Bianchi H, Palmer DA, Wood RH (2000) Conductivity of dilute aqueous electrolyte solutions at high temperatures and pressures using a flow cell. J Solution Chem 29: 217–235

1151 Ho PC, Palmer DA, Gruszkiewicz MS (2001) Conductivity measurements of dilute aqueous HCl
1152 solutions to high temperatures and pressures using a flow-through cell. J Phys Chem B 105:1260–
1153 1266
1154
1155 Ildefonse B, Blackman DK, John BE, Ohara Y, Miller DJ, MacLeod CJ (2007) Oceanic core
1156 complexes and crustal accretion at slow-spreading ridges. Geology 35: 623–626
1157
1158 Jaffey AH, Flynn KF, Glendenin LE, Bentley WT., Essling AM (1971) Precision measurement of
1159 half-lives and specific activities of ^{235}U and ^{238}U. Phys Rev C 4:1889
1160
1161 Jupp TE, Schultz A (2004) Physical balances in subseafloor hydrothermal convection cells. J
1162 Geophys Res-Sol Earth 109(B5)
1163
1164 Klein F, Bach W, Jöns N, McCollom T, Moskowitz B, Berquó T (2009) Iron partitioning and
1165 hydrogen generation during serpentinization of abyssal peridotites from 15 N on the Mid-Atlantic
1166 Ridge. Geochim Cosmochim Ac 73:6868–6893
1167
1168 Le Maitre RW (1982) Numerical Petrology, Statistical Interpretation of Geochemical Data.
1169 Elsevier, Amsterdam
1170
1171 Le Roux LJ, Glendenin LE (1963). Half-life of 232Th. In: Proceedings of the National Meeting on
1172 Nuclear Energy: Application of Isotopes and Radiation, Pretoria, pp 83–94
1173 Lombardo B, Pognante U (1982) Tectonic implications in the evolution of the Western Alps
1174 ophiolite metagabbros. Ofioliti 2:371–394
1175

1176 Lombardo B, Rubatto D, Castelli D (2002) Ion microprobe U-Pb dating of zircon from a Monviso
1177 metaplagiogranite: implications for the evolution of the Piedmont-Liguria Tethys in the Western
1178 Alps. Ofioliti 27:109–117
1179
1180 Ludwig K. R. (2012) User's manual for ISOPLOT 3.75, a geochronological toolkit for Microsoft
1181 Excel. Berkeley Geochronology Center, Spec. Pub. 5
1182
1183 Manatschal G, Müntener O (2009) A type sequence across an ancient magma-poor ocean–continent
1184 transition: the example of the western Alpine Tethys ophiolites. Tectonophysics 473:4–19
1185
1186 Manatschal G, Sauter D, Karpoff AM, Masini E, Mohn G, Lagabrielle Y (2011) The Chenaillet
1187 Ophiolite in the French/Italian Alps: an ancient analogue for an oceanic core complex? Lithos
1188 124:169–184
1189
1190 Marques AFA (2005) Geology and genesis of sulfide mineralization in the Rainbow ultramafic-
1191 hosted seafloor hydrothermal system. Dissertation, University of Lisbon
1192
1193 Marques AFA, Barriga FJ, Chavagnac V, Fouquet Y (2006) Mineralogy, geochemistry, and Nd
1194 isotope composition of the Rainbow hydrothermal field, Mid-Atlantic Ridge. Miner Deposita
1195 41:52–67
1196
1197 Marques AFA, Barriga FJ, Scott SD (2007) Sulfide mineralization in an ultramafic-rock hosted
1198 seafloor hydrothermal system: From serpentinization to the formation of Cu–Zn–(Co)-rich massive
1199 sulfides. Mar Geol 245:20–39
1200

Martin S, Rebay G, Kienast J, Mével C (2008) An eclogitised oceanic palaeo-hydrothermal field from the St. Marcel Valley (Italian Western Alps). Ofioliti 33:49–63

McCaig AM, Cliff RA, Escartin J, Fallick AE, MacLeod CJ (2007) Oceanic detachment faults focus very large volumes of black smoker fluids. Geology 35:935–938

McDonough WF, Sun S (1995) The composition of the Earth. Chem Geol 120:223–253

Melekestseva IY, Zaykov VV, Nimis P, Tret'yakov GA, Tessalina SG (2013) Cu–(Ni–Co–Au)-bearing massive sulfide deposits associated with mafic–ultramafic rocks of the Main Urals Fault, South Urals: Geological structures, ore textural and mineralogical features, comparison with modern analogs. Ore Geol Rev 52:18–36

Melekestseva IY, Tret'yakov GA, Nimis P, Yuminov AM, Maslennikov VV, Maslennikova SP, Kotlyarov VA, Beltenev VE, Danyushevsky LV, Large R (2014) Barite-rich massive sulfides from the Semenov-1 hydrothermal field (Mid-Atlantic Ridge, 13°30.87'N): Evidence for phase separation and magmatic input. Mar Geol 349:37–54

Mellini M, Rumori C, Viti C (2005) Hydrothermally reset magmatic spinels in retrograde serpentinites: formation of "ferritchromit" rims and chlorite aureoles. Contrib Mineral Petr 149:266–275

Merlini A, Grieco G, Diella V (2009) Ferritchromite and chromian-chlorite formation in mélange-hosted Kalkan chromitite (Southern Urals, Russia). Am Mineral 94:1459–1467

1226 Mével C (2003) Serpentinization of abyssal peridotites at mid-ocean ridges. C R Geosci 335:825–
1227 852
1228
1229 Montel JM, Foret S, Veschambre M, Nicollet C, Provost A (1996) Electron microprobe dating of
1230 monazite. Chem Geol 131:37–53
1231
1232 Nadoll P, Koenig AE (2011) LA-ICP-MS of magnetite: methods and reference materials. J Anal
1233 Atom Spectrom 26:1872–1877
1234
1235 Nadoll P, Angerer T, Mauk JL, French D, Walshe J (2014) The chemistry of hydrothermal
1236 magnetite: a review. Ore Geol Rev 61:1–32
1237
1238 Nadoll P, Mauk JL, Leveille RA, Koenig AE (2015) Geochemistry of magnetite from porphyry Cu
1239 and skarn deposits in the southwestern United States. Miner Deposita 50:493–515
1240
1241 Niu Y (2004) Bulk-rock major and trace element compositions of abyssal peridotites: implications
1242 for mantle melting, melt extraction and post-melting processes beneath mid-ocean ridges. J Petrol
1243 45:2423–2458
1244
1245 O'Neill HSC, Palme H (1998) Composition of the silicate Earth: implications for accretion and core
1246 formation. In: Jackson I (ed) The Earth's mantle: composition, structure and evolution, Cambridge
1247 University Press, pp. 3–126
1248
1249 Panseri M, Fontana E, Tartarotti P (2008) Evolution of rodingitic dykes: metasomatism and
1250 metamorphism in the Mount Avic serpentinites (Alpine Ophiolites, southern Aosta Valley). Ofioliti,
1251 33:165–185

Paraskevopoulos GM, Economou M (1980) Genesis of magnetite ore occurrences by metasomatism of chromite ores in Greece. Neues Jb Miner Abh 140:29–53

Paulick H, Bach W, Godard M., De Hoog JCM, Suhr G, Harvey J (2006) Geochemistry of abyssal peridotites (Mid-Atlantic Ridge, 15 20′ N, ODP Leg 209): implications for fluid/rock interaction in slow spreading environments. Chem Geol 234:179–210

Pester NJ, Ding K, Seyfried WE (2014) Magmatic eruptions and iron volatility in deep-sea hydrothermal fluids. Geology 42:255–258

Piccardo, G-B. (2008) The Jurassic Ligurian Tethys, a fossil ultraslow-spreading ocean: the mantle perspective. In: Coltorti M, Grégoire M (Eds) Metamorphism in oceanic and continental lithospheric mantle. Geological Society, London, Special Publication, vol. 293, pp. 11–33

Polino R, Martin S, Malusà M, Mosca P, Bonetto F, Baggio P, Baster I, Bertolo D, Carraro F, Fontan D, Gianotti F, Monopoli B, Perello P, Schiavo A, Venturini G, Vuillermoz R (2014) Note illustrative della carta geologica d'Italia alla scala 1:50.000 Aosta F. 90. Ispra-Servizio Geologico d'Italia

Puteanus D, Glasby GP, Stoffers P, Kunzendorf H (1991) Hydrothermal iron-rich deposits from the Teahitia-Mehitia and Macdonald hot spot areas, Southwest Pacific. Mar Geol 98:389–409

Renna MR, Tribuzio R (2011) Olivine-rich troctolites from Ligurian ophiolites (Italy): evidence for impregnation of replacive mantle conduits by MORB-type melts. J Petrol 52:1763–1790

Rollinson H (1993) Using geochemical data. Longman, London

Rona PA (1988) Hydrothermal mineralization at oceanic ridges. Can Mineral 26:431–465

Rossetti P, Gatta GD, Diella V, Carbonin S, Della Giusta A, Ferrario A (2009) The magnetite ore districts of the southern Aosta Valley (Western Alps, Italy): a mineralogical study of metasomatized chromite ore. Mineral Mag 73:737–751

Routhier P (1963) Les gisements métallifères: géologie et principes de recherche. Masson, Paris

Sanfilippo A, Tribuzio R (2013) Building of the deepest crust at a fossil slow-spreading centre (Pineto gabbroic sequence, Alpine Jurassic ophiolites). Contrib Mineral Petr 165:705–721

Sanfilippo A, Tribuzio R, Tiepolo M (2014) Mantle–crust interactions in the oceanic lithosphere: Constraints from minor and trace elements in olivine. Geochim Cosmochim Ac 141:423–439

Sawyer GM, Oppenheimer C, Tsanev VI, Yirgu G (2008) Magmatic degassing at Erta'Ale volcano, Ethiopia. J Volcanol Geoth Res 178:837–846

Schmid SM, Fügenschuh B, Kissling E, Schuster R (2004) Tectonic map and overall architecture of the Alpine orogen. Eclogae Geol Helv 97:93–117

Schwartz S, Guillot S, Reynard B, Lafay R, Debret B, Nicollet C, Lanari P, Auzende AL (2013) Pressure–temperature estimates of the lizardite/antigorite transition in high pressure serpentinites. Lithos 178:197–210

1304 Seyfried Jr WE (1987) Experimental and theoretical constraints on hydrothermal alteration
1305 processes at mid-ocean ridges. Annu Rev Earth Pl Sc 15:317
1306
1307 Seyfried WE, Foustoukos DI, Allen DE (2004) Ultramafic-hosted hydrothermal systems at
1308 mid-ocean ridges: chemical and physical controls on pH, redox and carbon reduction reactions. In:
1309 German CR, Lin J, Parson LM (eds) Mid-ocean ridges: hydrothermal interactions between the
1310 lithosphere and oceans, American Geophysical Union, Washington, DC, pp. 267–284
1311
1312 Seyfried WE, Pester N, Fu Q (2010) Phase equilibria controls on the chemistry of vent fluids from
1313 hydrothermal systems on slow spreading ridges: reactivity of plagioclase and olivine solid solutions
1314 and the pH-silica connection. In: Rona PA, Devey CW, Dyment J, Murton BJ (eds) Diversity of
1315 hydrothermal systems on slow spreading ocean ridges, American Geophysical Union, Washington,
1316 DC, pp. 297-320
1317
1318 Seyfried WE, Pester NJ, Ding K, Rough M (2011) Vent fluid chemistry of the Rainbow
1319 hydrothermal system (36 N, MAR): phase equilibria and in situ pH controls on subseafloor
1320 alteration processes. Geochim Cosmochim Ac 75:1574–1593
1321
1322 Singh SC, Crawford WC, Carton H, Seher T, Combier V, Cannat M, Canales JP, Düsünür D,
1323 Escartin J, Miranda JM (2006). Discovery of a magma chamber and faults beneath a Mid-Atlantic
1324 Ridge hydrothermal field. Nature 442:1029–1032
1325
1326 Suhr G, Hellebrand E, Johnson K, Brunelli D (2008) Stacked gabbro units and intervening mantle:
1327 A detailed look at a section of IODP Leg 305, Hole U1309D. Geochem Geophy Geosy 9
1328

Szitkar F, Dyment J, Fouquet Y, Honsho C, Horen H (2014) The magnetic signature of ultramafic-hosted hydrothermal sites. Geology 42:715–718

Stampfli GM (2000) Tethyan oceans. Geol Soc Spec Publ 173:1–23

Stella A (1916) Le miniere di Cogne (Val d'Aosta). S.A.I.G. A. Barabino, Genova

Tartarotti P, Festa A, Benciolini L, Balestro G (2015) Mantle-cover sequence in the Western Alps metaophiolites: a key to recognize remnants of an exhumed Oceanic Core Complex (OCC). Rend Online Soc Geol It, Suppl. n. 2, Vol. 35

Tivey MA, Dyment J (2010) The magnetic signature of hydrothermal systems in slow spreading environments. In: Diversity of Hydrothermal Systems on Slow Spreading Ocean Ridges. In: Rona PA, Devey CW, Dyment J, Murton BJ (eds) Diversity of hydrothermal systems on slow spreading ocean ridges, American Geophysical Union, Washington, DC, pp. 43–66

Tumiati S, Martin S, Godard G (2010) Hydrothermal origin of manganese in the high-pressure ophiolite metasediments of Praborna ore deposit (Aosta Valley, Western Alps). Eur J Mineral 22:577–594

Tumiati S, Godard G, Martin S, Malaspina N, Poli S (2015) Ultra-oxidized rocks in subduction mélanges? Decoupling between oxygen fugacity and oxygen availability in a Mn-rich metasomatic environment. Lithos 226:116–130

Von Damm KL (2004) Evolution of the hydrothermal system at East Pacific Rise 9°50'N: geochemical evidence for changes in the upper oceanic crust. In: German CR, Lin J, Parson LM

(eds) Mid-ocean ridges: hydrothermal interactions between the lithosphere and oceans, American Geophysical Union, Washington, DC, pp. 285–304

Werner CD (1997). Data report: geochemistry of rocks and minerals of the gabbro complex from the Kane area (MARK). In: Karson JA, Cannat M, Miller DJ, Elthon D (eds) Proceedings of the Ocean Drilling Program. Scientific Results (Vol. 153). Ocean Drilling Program, pp. 457–470

Whitney DL, Evans BW (2010) Abbreviations for names of rock-forming minerals. Am Mineral 95:185–187

Wolery TJ, Jarek RL (2003) Software User's Manual EQ3/6 (Version 8.0). Sandia National Laboratories, Albuquerque, New Mexico

Wolery TJ (2013) EQ3/6 - Software for Geochemical Modeling, Version 8.0a. Lawrence Livermore National Laboratory, Livermore, California

Yıldırım N, Dönmez C, Kang J, Lee I, Pirajno F, Yıldırım E, Günay K, Seo JH, Farquhar J, Chang, SW (2016) A magnetite-rich Cyprus-type VMS deposit in Ortaklar: A unique VMS style in the Tethyan metallogenic belt, Gaziantep, Turkey. Ore Geol Rev 79:425–442

Figure captions

Fig. 1. Geological map of the southern Valle d'Aosta region. Redrawn and modified after De Giusti et al. (2003) and Dal Piaz et al. (2010).

Fig. 2. a) Simplified geologic map of the Cogne mining district showing the structural relationships between the Cogne serpentinite and the associated units. Numbered stars indicate the sampling sites (see text for details). Units after Dal Piaz et al. (2010); digital terrain map (DTM) from "Agenzia Regionale per la Protezione Ambientale" (ARPA) Piemonte. b) Geological profile through the Cogne serpentinite. Redrawn and modified after Elter (1971). c) Pseudostratigraphic columns of the three sampling sites.

Fig. 3. Typical magnetite ore and rock samples from Site 1 (a, b, e), Site 2 (c) and Site 3 (d, f). a) Nodular ore sample, showing leopard (lower left corner), harristic (cm-sized iso-oriented rods of magnetite in the centre) and massive (upper portion) texture. The light matrix is serpentine (+ brucite + olivine). b) Massive ore, with minor serpentine gangue. Arrows indicate rounded magnetite crystals. c) Deformed magnetite (+ chalcopyrite + antigorite) vein (outlined by dashed lines) in serpentinized peridotite. Chalcopyrite is completely weathered into Fe-oxyhydroxides and secondary copper minerals. The pen is 14 cm-long. d) Fine-grained leopard ore in diopside gangue. e) Magnetite-poor pegmatoid serpentinite. Note the presence of dark and light interlobate domains. The former are composed of antigorite and minor magnetite, the latter are formed by antigorite only. f) Contact between a magnetite-rich diopsidite (left) and a pegmatoid serpentinite (right) with amoeboid magnetite-rich domains (light grey) interweaved with magnetite-free domains. Dark antigorite coronae contour the two domains. Magnetite content increases in the right part of the sample, but embayed boundaries are still recognizable. Cut and polished sample.

Fig. 4. Microstructural features in Cogne rocks. a) Magnetite poikiloblast in leopard ore from Site 1, showing indented boundaries with antigorite. Inclusions in magnetite are clinochlore (usually anhedral), brucite (small and euhedral) and antigorite (large euhedral crystals). Gangue is antigorite with minor calcite, which forms late impregnations and thin veins. Back-scattered electron (BSE) image. b) Nearly massive fine-grained disseminated ore from Site 2. Magnetite (white) is associated with acicular diopside (grey) and forms a corona around an antigorite (dark grey) bastite. Reflected plane-polarized light. c) Fine-grained disseminated ore from Site 2. Magnetite (white), antigorite (black) and diopside (medium grey) replace former silicates, but bastite sites (round black areas) and Mg-Al-rich chromites (framed; see Fig. 4d for a close-up) are still preserved. BSE image. d) Mg-Al-rich chromite crystal (medium gray), partly altered along the rims and fractures into Fe-rich chromite (light grey) + Cr-rich chlorite (black) and mantled by magnetite, intergrown with antigorite (black) and diopside (dark grey). e) Magnetite + chalcopyrite patch associated with antigorite in a dismembered vein from Site 2. Bluish inclusions in magnetite are bornite. Antigorite occurs both within and around the magnetite, forming indented boundaries with it. Reflected plane-polarized light. f) Euhedral magnetite crystals in a diopside-rich portion of a leopard ore sample from Site 3. Diopside forms randomly-oriented subhedral prismatic crystals (medium gray) with interstitial antigorite (dark grey). Black mineral included in magnetite or interstitial between diopside crystals (right) is clinochlore. BSE image. g) Serpentinized pegmatoid ultramafic rock from Site 3 (see Fig. 3f), showing interlobate domains separated by coronae structures. Transmitted light, crossed polars. h) Enlargement of framed area in c). Light-coloured domain (upper left) is composed of coarse-grained interlocking antigorite; dark domain (right) is made up of isotropic lizardite, clinochlore (anomalous brown interference colour), antigorite (white-light grey) and magnetite (opaque). Fine-grained interlocking antigorite lines the boundary between the two domains. Transmitted light, crossed polars (upper) and plane polarized light (lower). Mineral abbreviations (after Whitney and Evans, 2010) - Mag: magnetite; Atg: antigorite; Clc: clinochlore;

Brc: brucite; Cal: calcite; Di: diopside; Lz: lizardite; Ccp: chalcopyrite; Bn: bornite; Chr: chromite; Chl: chlorite.

Fig. 5. Covariation of Co/Ni ratio and Cr content vs Fe_2O_3 content in Cogne rocks (this work and Carbonin et al., 2014) and ores. Data for abyssal peridotites after Niu (2004), Paulick et al. (2006), Andreani et al. (2014) are shown for comparison.

Fig. 6. Uraninite microstructural features and U-Th-Pb dating. a-d) Uraninite in Site 1 leopard ore and related dating [b) and c) from the same ore sample]. e-f) Aggregate of uraninite crystals in Site 1 leopard ore and related dating. Chemical map shows a U-rich rim. g-h) Inclusion-rich (magnetite, dark grey; clinochlore, black) uraninite crystal in Site 3 leopard ore and related dating. The chemical map reveals a homogeneous composition. i) Combination of all single-spot ages. Images and maps were obtained by SEM-BSE and EPMA, respectively. Geochronological data plotted using ISOPLOT (v. 3.75) Visual Basic add-in for Excel® (Ludwig, 2012). MSWD: mean square of weighted deviates.

Fig. 7. Electron microprobe traverses across uraninite crystals (see Fig. 6 for their position). Horizontal dashed lines indicate PbO plateau.

Fig. 8. Box and whiskers plot of magnetite trace element composition.

Fig. 9. Robust-PCA of magnetite trace element composition. Coordinates of datapoints (scores) are on left and lower horizontal axes. Coordinates of variables (loadings) are on right and upper horizontal axes.

Fig. 10. Co vs. Ni relationships in magnetite. Regression line (dashed) for magnetite-rich samples from Site 1 and 3 shows linear relationship between Co and Ni.

Fig. 11. Variation in pH, f_{O_2} and element concentrations in modified seawater equilibrated with harzburgite (a) or Fe-gabbro (b) at 400°C at various W/R.

Fig. 12. Mineral assemblages and variation in f_{O_2} produced by reaction of model hydrothermal fluids with selected rock types. Harzburgite-reacted fluid reacting with rocks at a) 300°C and 500 bar b) 400°C and 500 bar. Fe-gabbro-reacted fluid reacting with rocks at c) 300°C and 500 bar d) 400°C and 500 bar.

Fig. 13. Compositions of Cogne magnetites plotted in the discrimination diagram by Dare et al. 2014. Magnetites with Cr contents above detection limit are circled. The other data points are plotted assuming a Cr value equal to the detection limit of 8 ppm. Although this may have unduly shifted the points to lower Ni/Cr ratios, the strong hydrothermal character of the Cogne magnetites remains evident.

Fig. 14. Compositions of Cogne magnetites in the discrimination diagram of Dupuis and Beaudoin 2011. LA-ICP-MS data are not available for Al (generally <<0.1 wt% based on EPMA data), therefore the plotted (Mn+Al) contents should be considered as minimum values.

Fig. 15. Interpreted schematic evolution of the Cogne deposit. a) Formation of an oceanic core complex made up of mantle peridotites intruded by gabbros and Fe-gabbros, and locally impregnated by melts. Early circulation of hydrothermal fluids produces extensive serpentinization at relatively low-T (lizardite stability field). High water/rock ratios are possibly attained thanks to fluid focussing along fractures and faults. b) Convective circulation of seawater produces high-T

hydrothermal fluids that leach metals from harzburgites and Fe-gabbros. These fluids undergo phase separation and produce a magnetite-rich body at depth and a sulphide mound on the seafloor. A magnetite-sulphide stockwork zone marks the transition between the magnetite orebody and the sulphide mound. c) Close-up of the framed region in b). Phase separation produces an H_2S-rich vapour that quickly escapes from the system and a dense metal-rich brine. Then, the upwelling brine reacts with the serpentinites at various fluid/rock ratios and precipitates magnetite, producing fine-grained disseminated, nodular and replacive massive ores. Further upwelling of the magnetite-saturated fluids along fractures produces magnetite + chalcopyrite veins (stockwork zone) and fine-grained disseminations in shallower serpentinites.

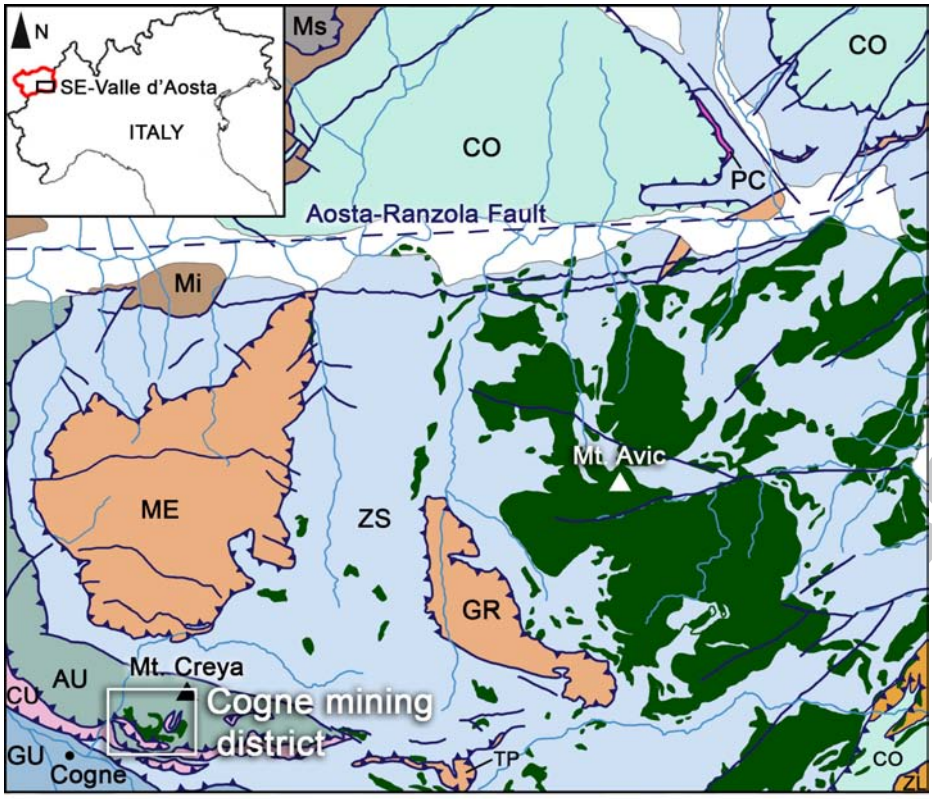

CONTINENTAL CRUST UNITS (i.e. Austroalpine)

ECLOGITIC

ME: Mont Emilius Unit
GR: Glacier-Rafray Unit
TP: Tour Ponton Unit

NON-ECLOGITIC

Ms: Upper Mont Mary Unit
Mi: Lower Mont Mary Unit

SESIA LANZO ZONE (ZL)

OPHIOLITIC UNITS

ECLOGITIC

ZS: Zermatt-Saas Unit
GU: Grivola-Urtier Unit

NON-ECLOGITIC

AU: Aouliletta Unit
CO: Combin Unit

Serpentinites

CONTINENTAL MARGIN UNITS

CU: Cogne Unit
PC: Pancherot-Cime Bianche Unit

Fault

Thrust fault

1491

1492

1493

1494 Fig. 1

1495

1496

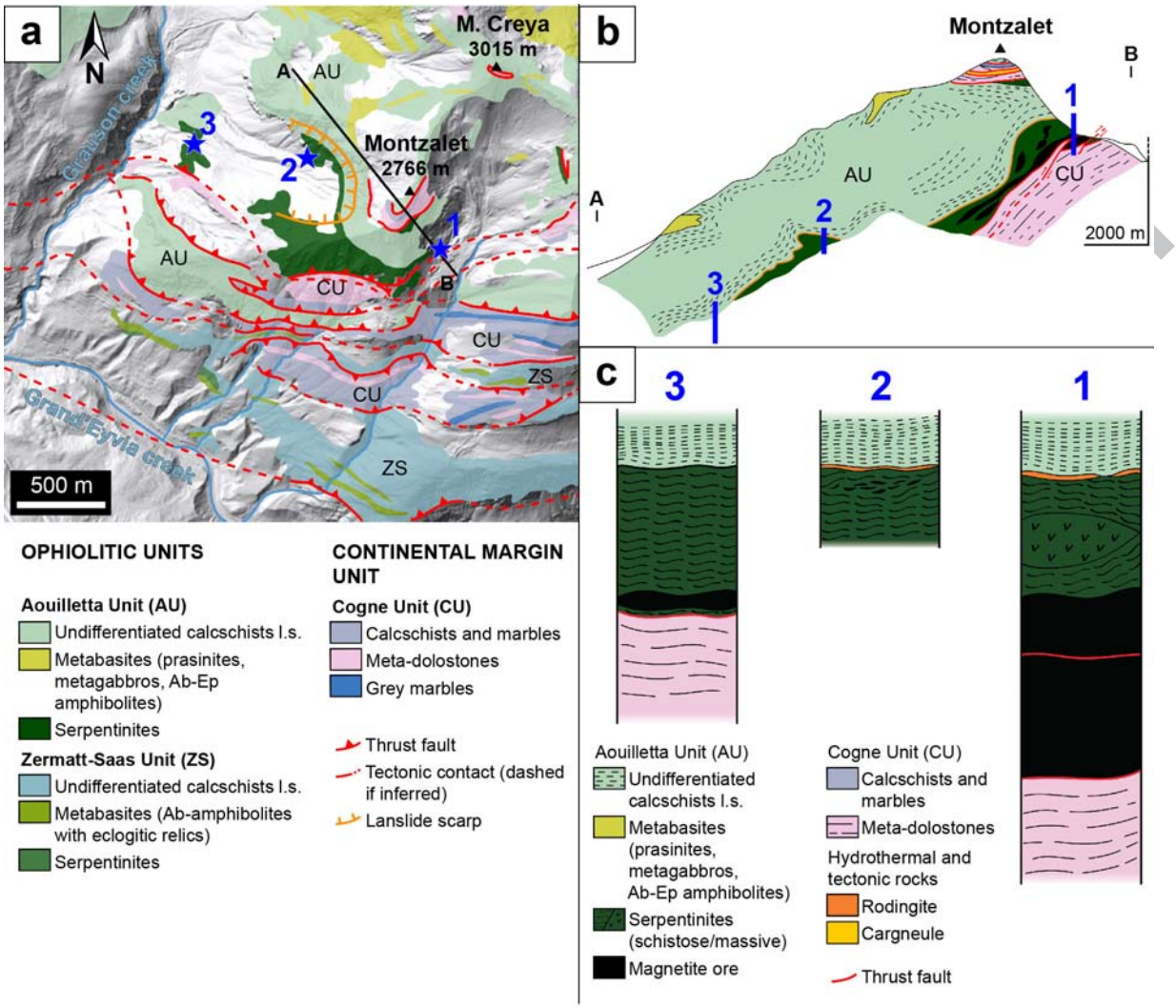

Fig. 2

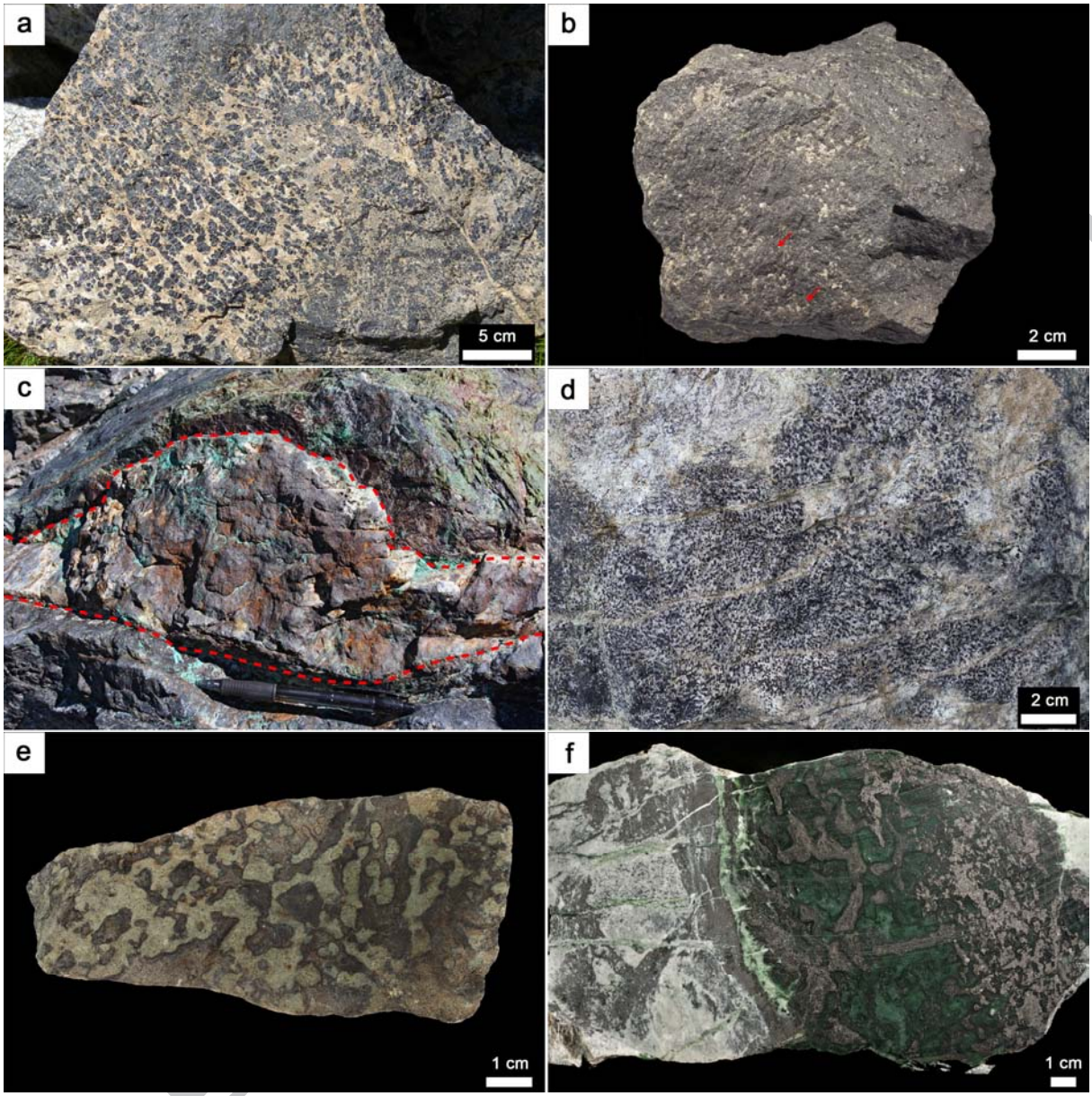

Fig. 3

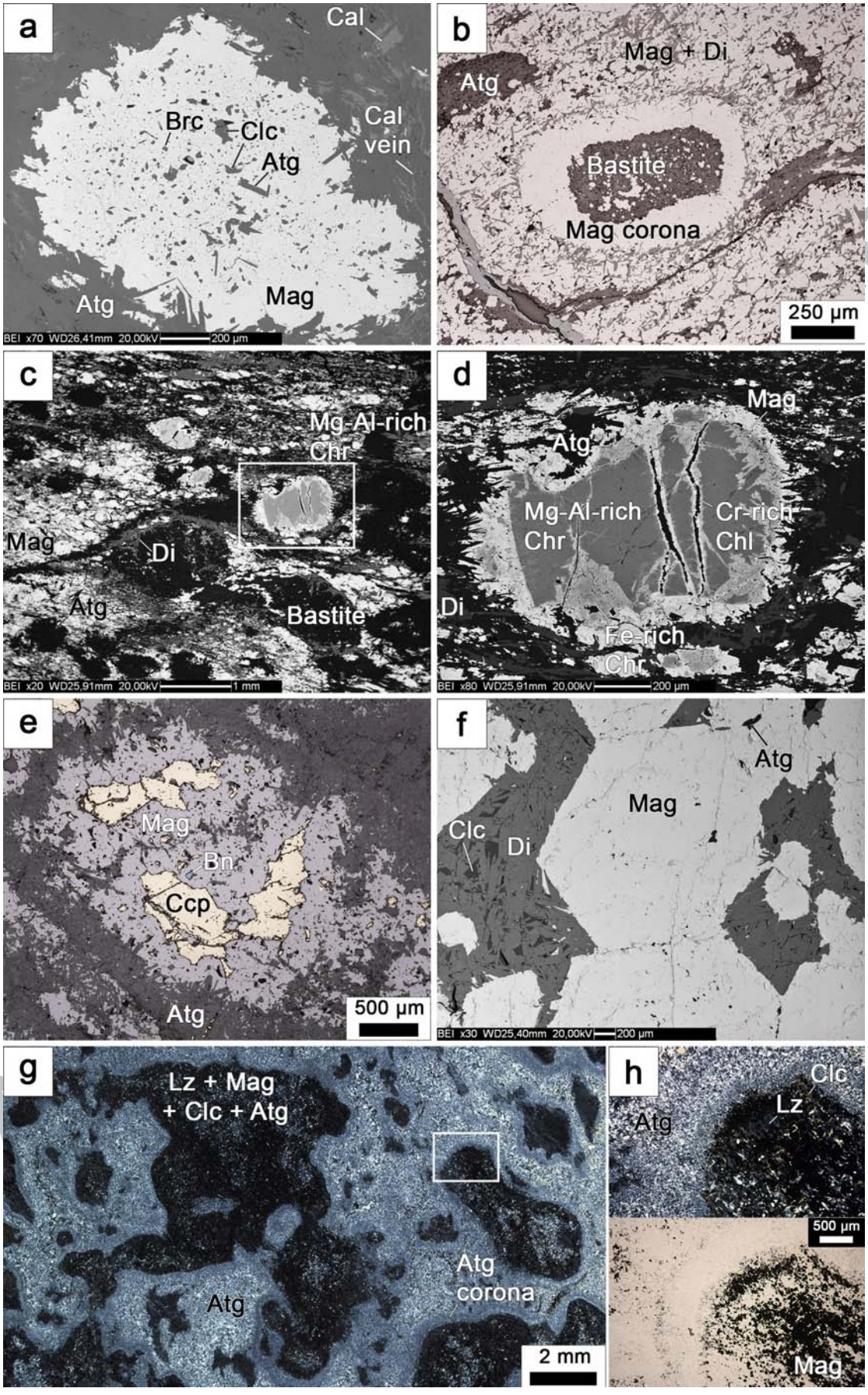
a
Cal
Brc
Clc
Atg
Cal vein
Atg
Mag
BEI x70 WD26,41mm 20,00kV 200 µm
b
Mag + Di
Atg
Bastite
Mag corona
250 µm
c
Mg-Al-rich Chr
Mag
Di
Atg
Bastite
BEI x20 WD25,91mm 20,00kV 1 mm
d
Mag
Atg
Mg-Al-rich Chr
Cr-rich Chl
Di
Fe-rich Chr
BEI x80 WD25,91mm 20,00kV 200 µm
e
Mag
Bn
Ccp
Atg
500 µm
f
Atg
Mag
Clc
Di
BEI x30 WD25,40mm 20,00kV 200 µm
g
Lz + Mag + Clc + Atg
Atg
Atg corona
2 mm
h
Clc
Lz
Atg
500 µm
Mag

1510

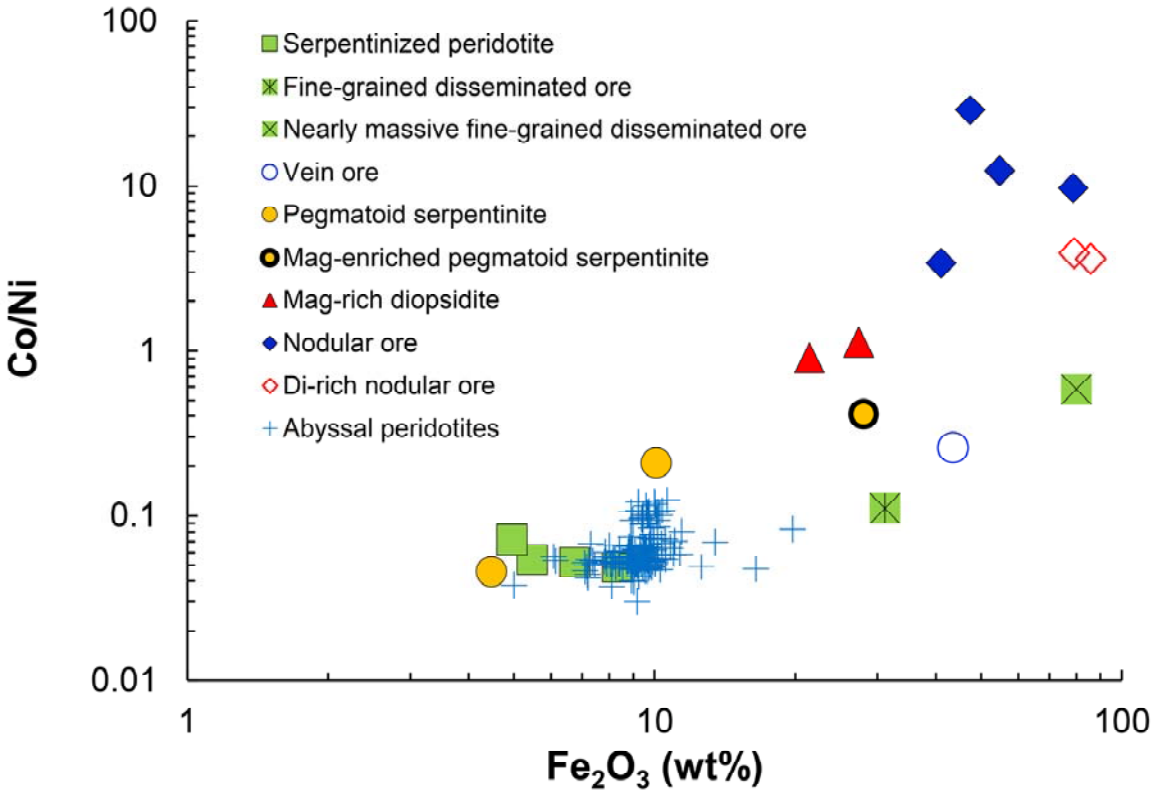

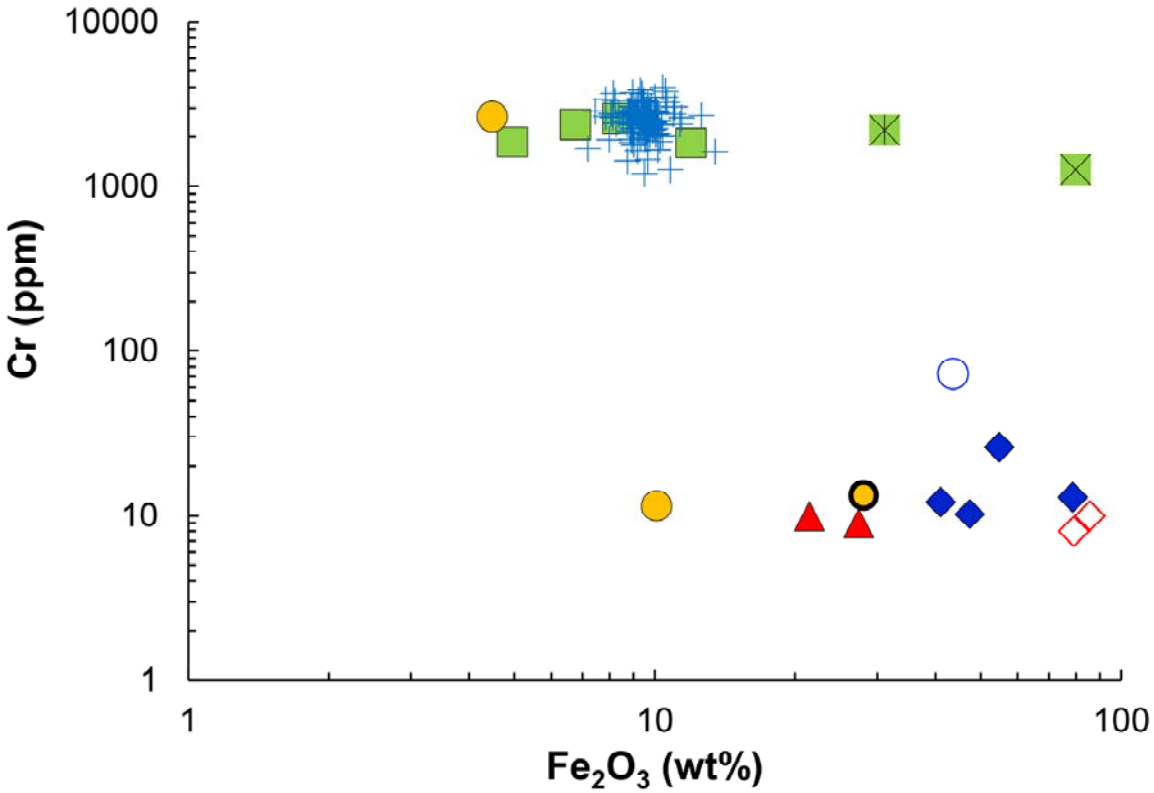

1511

1512

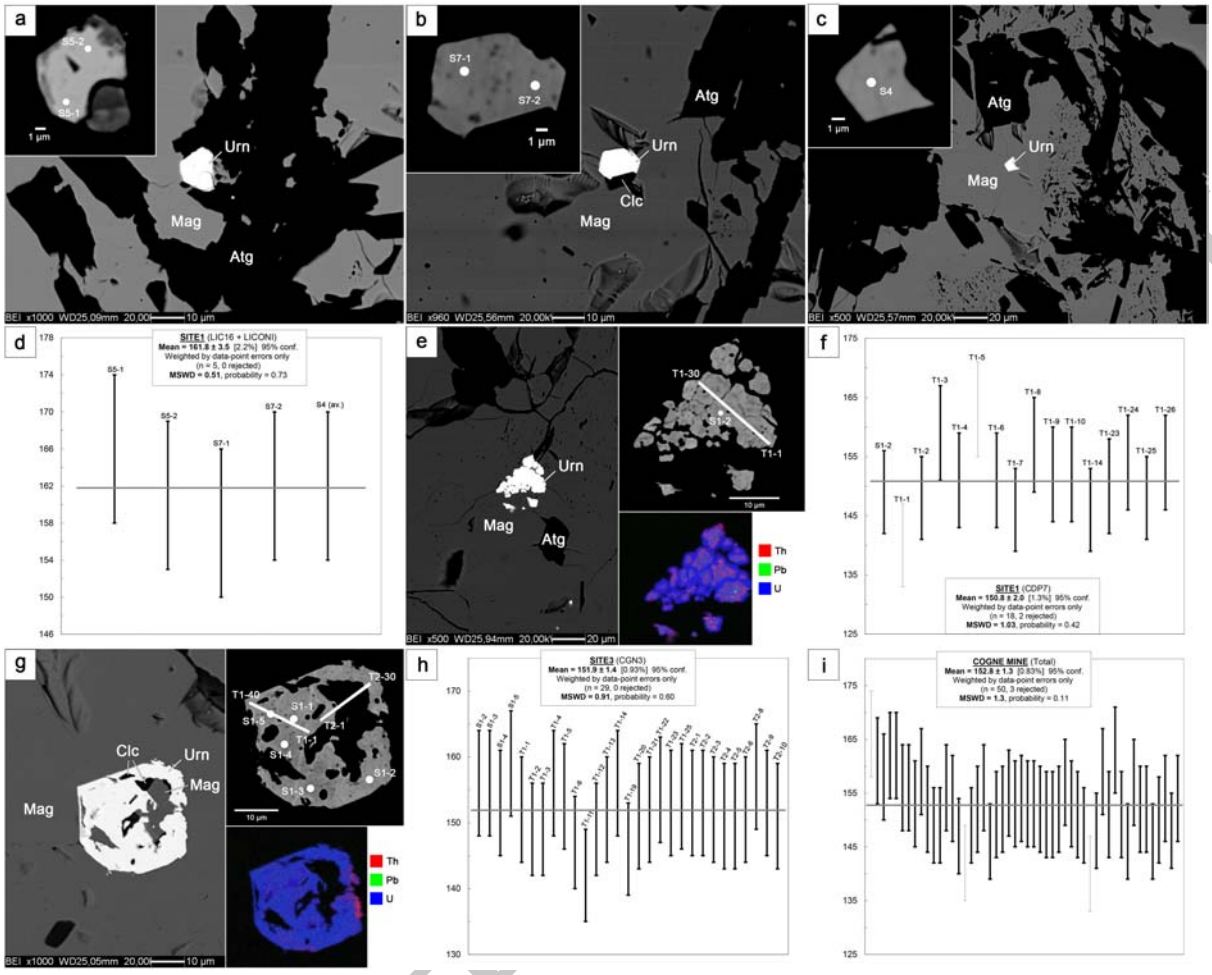

Fig. 6

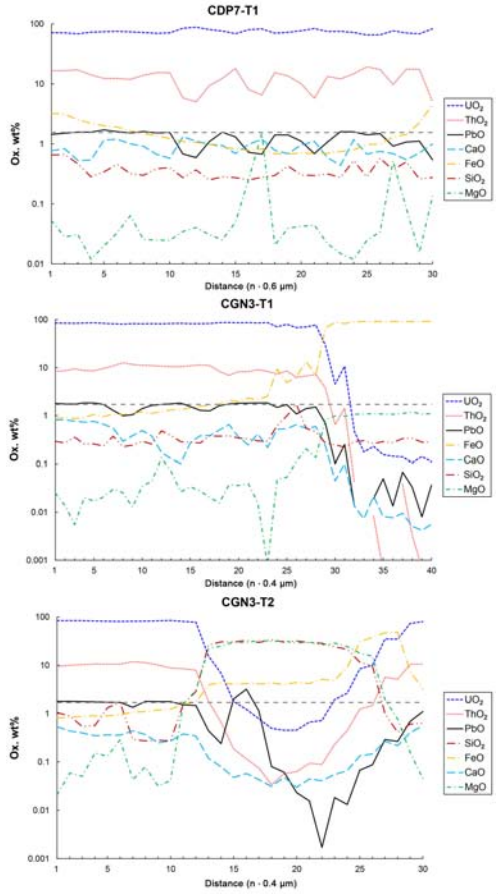

1519

1520

1521 Fig. 7

1522

1523

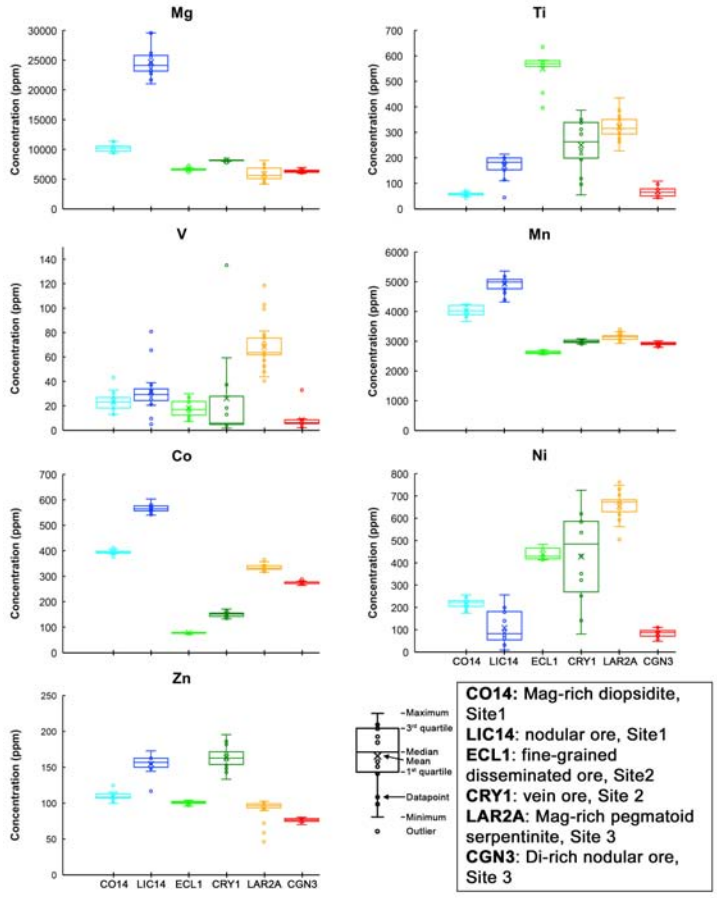

1524

1525

1526

1527

1528 Fig. 8

1529

1530

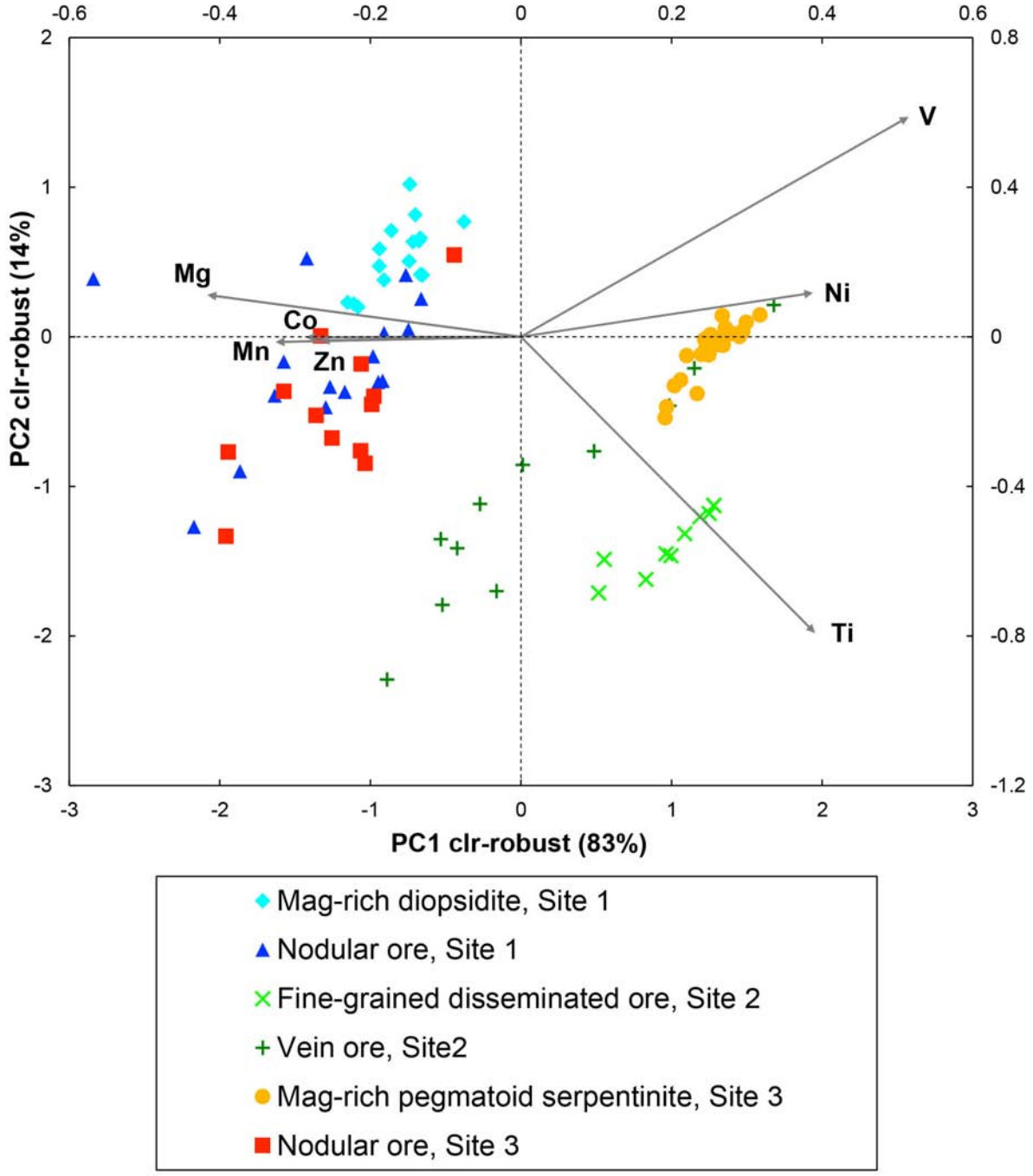

1531

1532

1533 Fig. 9

1534

1535

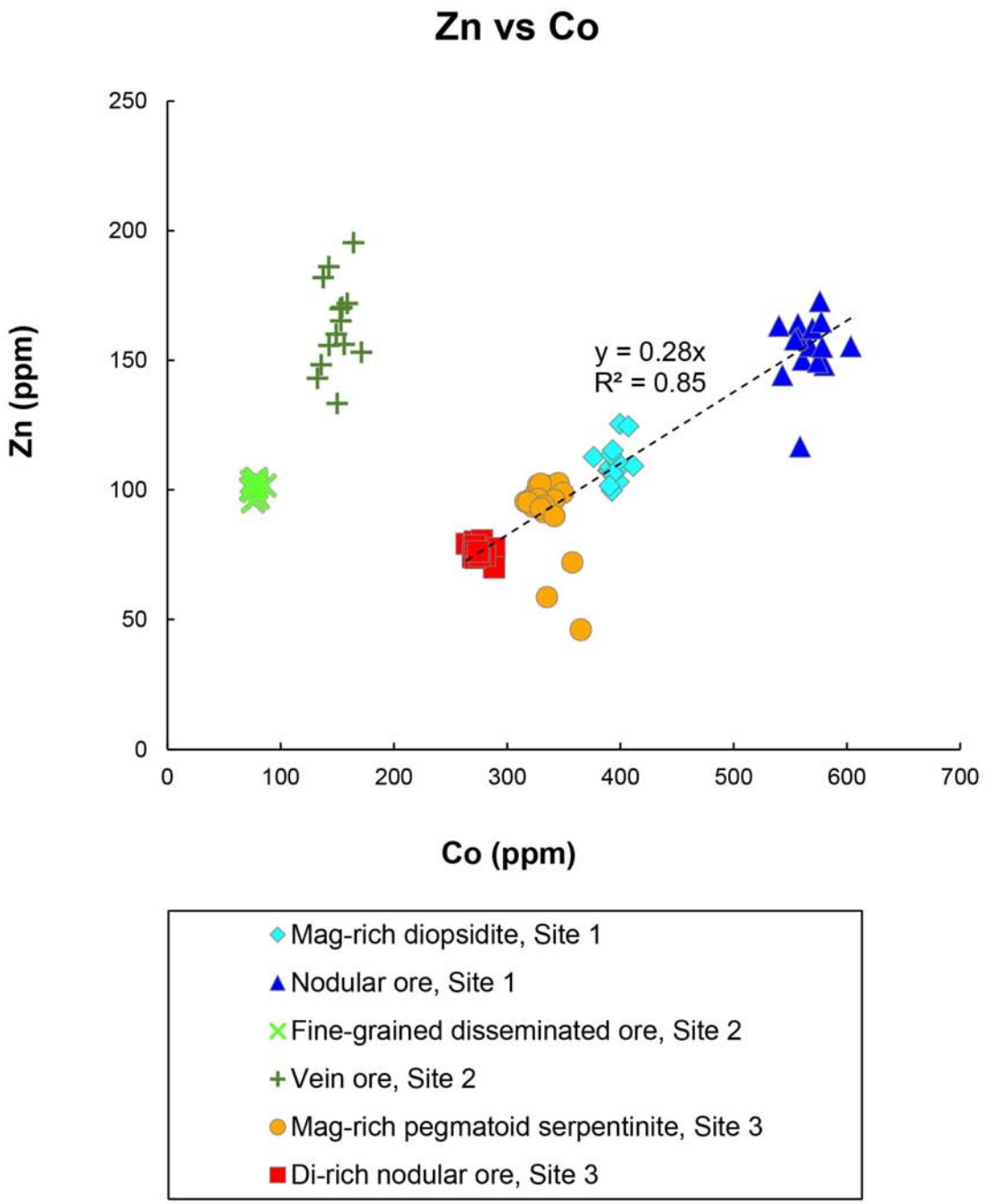

Fig. 10

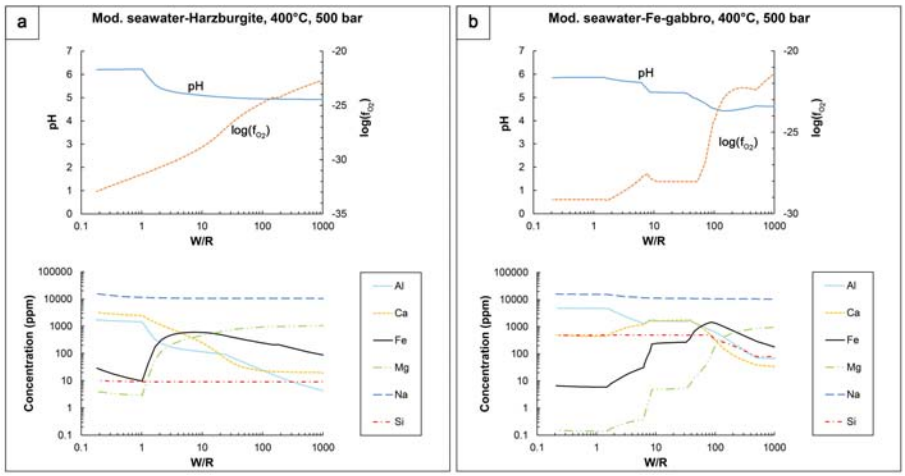

1542

1543

1544 Fig. 11

1545

1546

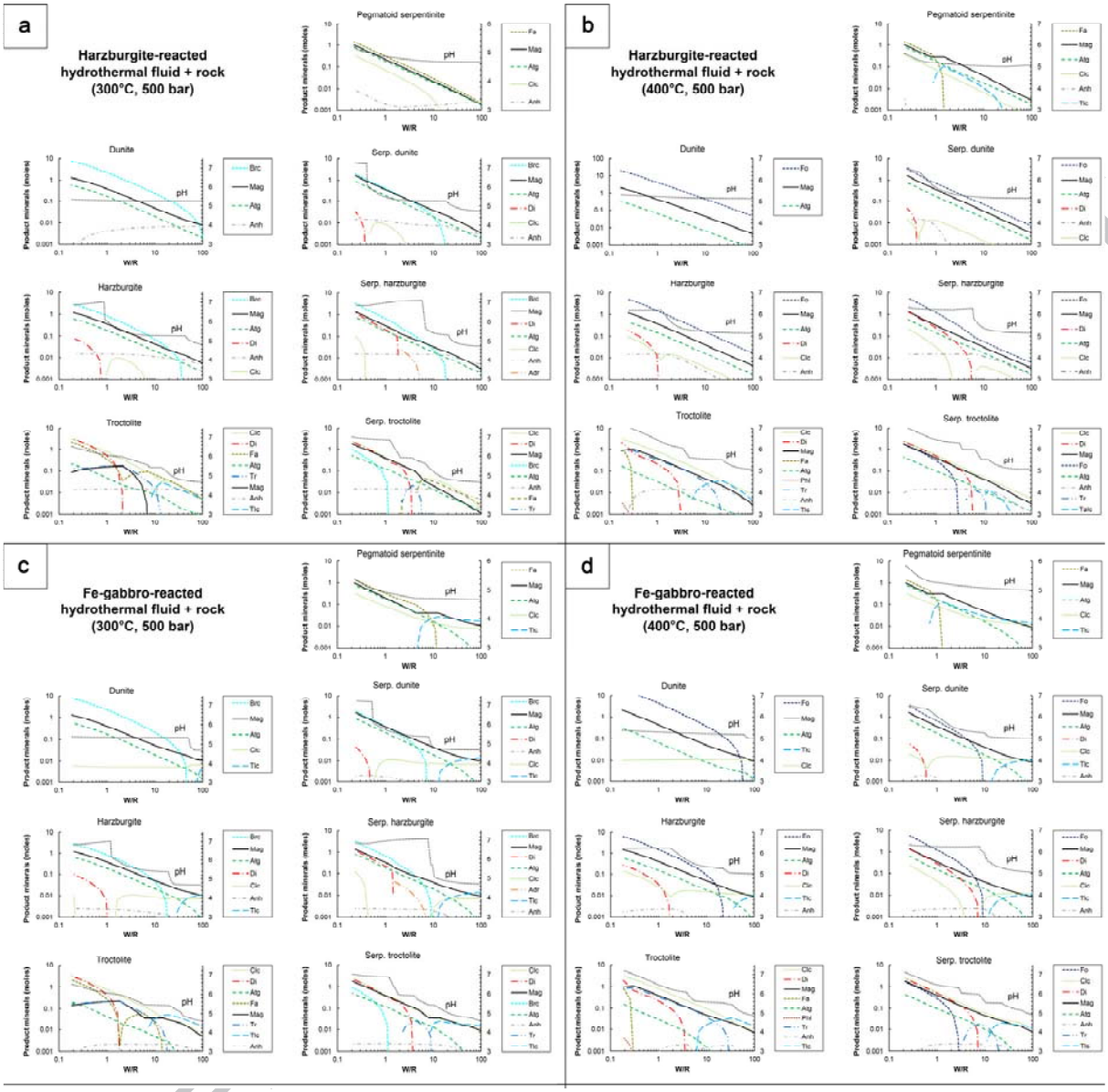

Fig. 12

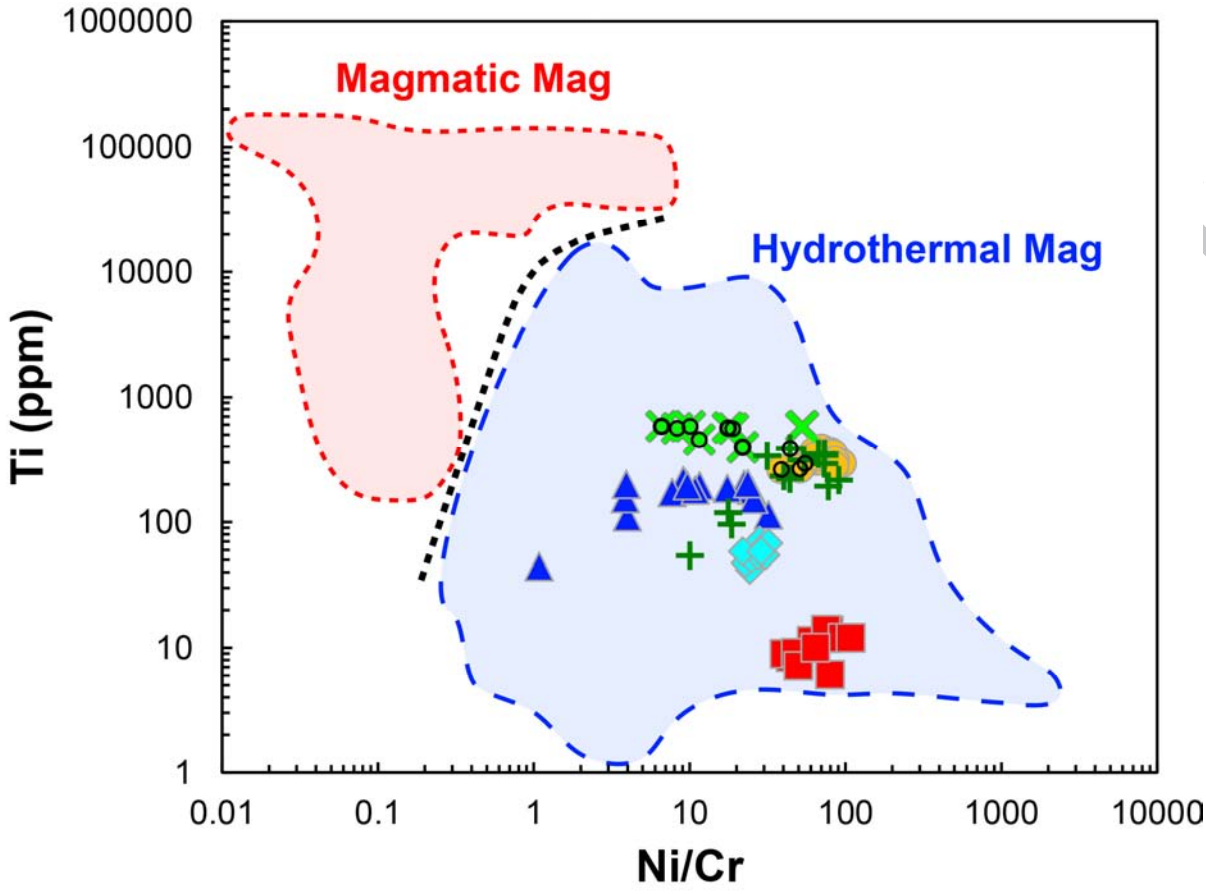

Fig. 13

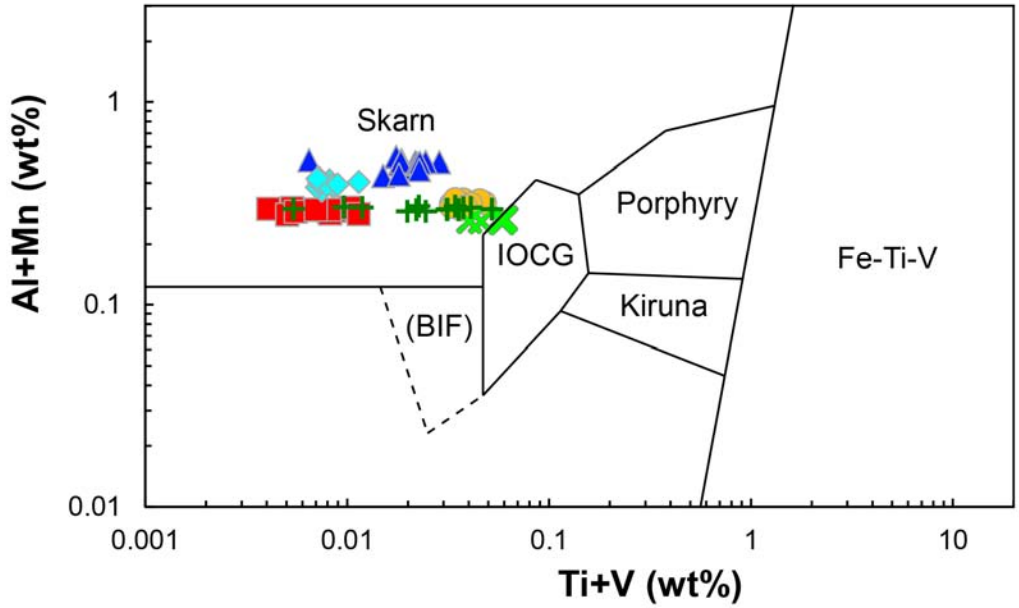

Fig. 14

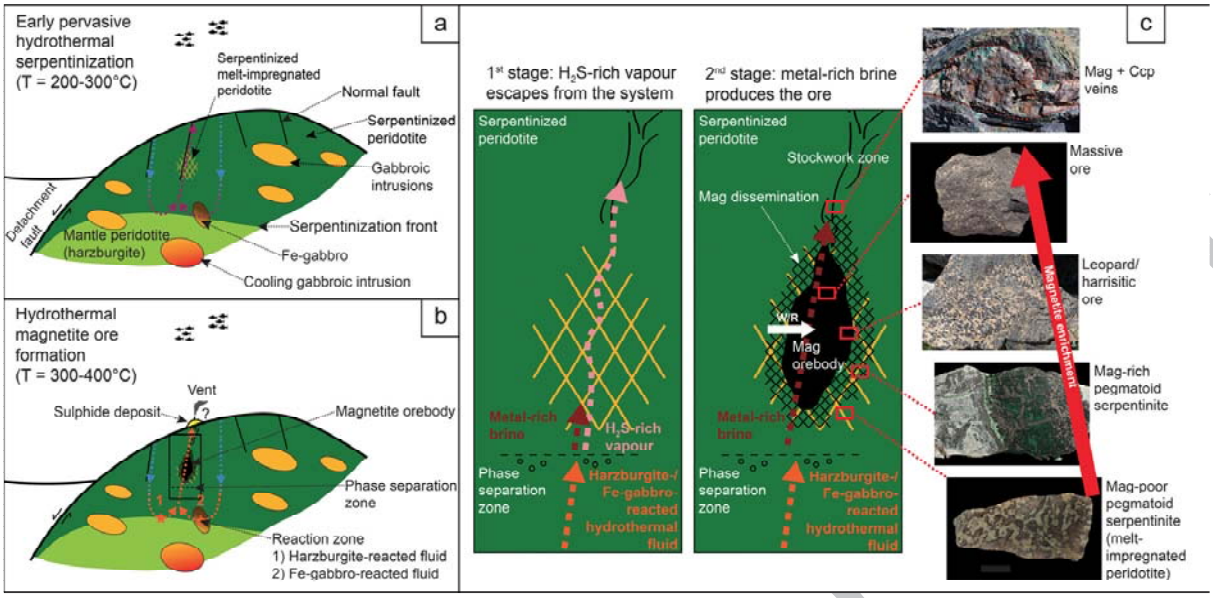

1566

1567

1568

1569 Fig. 15

1570

1571

1572

Table 1

Seawater composition*

Na^+	464.0
Cl^-	546.0
$HCO3^-$	2.34
Ca^{2+}	10.2
Mg^{2+}	53.0
K^+	9.8
$SiO_{2(aq)}$	0.11
Fe^{2+}	0.0000015
Al_{3+}	0.000037
SO_4^{2-}	28.2
$O_{2(aq)}$	0.25
pH	7.8

* After Klein et al. (2009).

Table 2

Rock compositions used in thermodynamic modelling.

Rock Type	Fe-gabbro[1]	Dunite[1]	Serp. Dunite[2]	Harzburgite[1]	Serp. Harzburgite[2]	Pegmatoid serpentinite[3]	Troctolite[1]	Serp. Troctolite[4]
Ox. wt%								
SiO_2	47.94	40.87	39.24	44.31	39.38	40.97	42.90	37.95
Al_2O_3	12.19	0.00	0.19	0.42	0.59	0.78	9.58	6.12
FeO	18.87	9.77	7.57	8.97	6.61	9.23	9.06	8.44
MgO	4.85	49.35	38.79	45.81	38.37	37.26	32.39	34.73
CaO	13.17	0.00	0.08	0.48	1.69	0.04	5.39	2.87
Na_2O	2.99	0.00	0.13	0.00	0.05	0.00	0.67	0.41
H_2O	0.00	0.00	13.99	0.00	13.30	11.72	0.00	9.47
Tot.	100.00	100.00	100.00	100.00	100.00	100.00	100.00	100.00

[1] "Artificial" rock.

[2] Andreani et al. (2014).

[3] Sample CDP15, Site 1.

[4] Sanfilippo et al. (2014).

1576

1577

Table 3

EPMA mineral compositions.

Location	Site 1	Site 1	Site 2	Site 3	Site 3
Sample	LIC12	LIC 14, LIC 15	ECL1	LAR4A	LAR2C
Rock type	Serpentinized peridotite	Nodular ore	Fine-grained disseminated ore	Serpentinized peridotite	Mag-rich diopsidite
Mineral	Antigorite	Spinel comri	Magnetite	Antigorite	Lizardite	Forsterite	Brucite	Included	Clinochlore	Ti-rich chondrodite	Magnetite	Antigorite	Bastite	Veined	Diopside	Lizardite	Spinel comri	Magnetite	Antigorite	Lizardite	Clinochlore	Magnetite	Diopside
Ad				Included		Included																	Fine-

ditional information			re	ddle	m					d in Mag^2				ed in Mag						ed in Mag		d in Mag							e		in					re	ddle	m										grained	
			Mg-Al-rich chromite	Fe-rich chromite	Magnetite																								core	rim					Mg-Al-rich chromite	Fe-rich chromite	Magnetite											
Ox. wt%	Mean (6)	s_1				Mean (9)	s	Mean (22)	s	Mean (5)	s	Mean (9)	s	Mean (4)	s	Mean (6)	s	Mean (5)	s	Mean (10)	s	Mean (19)	s				Mean (3)	s										Mean (4)	s	Mean (6)	s		Mean (5)	s	Mean (8)	s	Mean (5)	s
SiO_2	42.80	2.03	0.00	0.34	0.01	0.13	0.20	44.69	0.58	44.55	0.53	37.99	2.06	38.84	0.88	41.55	1.65	3.62	2.14	0.46	1.29	33.97	1.27	34.89	34.73	0.07	44.72	0.30	45.56	43.70	44.59	55.98	41.68	41.22	0.03	2.42	0.12	0.03	0.02	43.78	0.32	39.38	35.63	0.47	0.16	0.21	55.42	0.36
TiO	0.	0.	0.	0.	0.	0.	0.	0.	0.	0.	0.	0.	0.	0.	0.	0.	0.	0.	0.	0.	0.	0.	0.	5.	5.	0.	0.	0.	0.	0.	0.	0.	0.	0.	0.	0.	0.	0.	0.	0.	0.	0.	0.	0.	0.	0.	0.	0.

$_2$	01	02	03	14	01	01	02	01	01	02	01	02
Al_2O_3	1.00	0.51	25.73	0.62	0.00	0.04	0.04	0.57	0.26	0.79	0.41	4.65
Cr_2O_3	0.44	0.16	43.72	38.69	3.51	0.01	0.01	0.01	0.01	0.02	0.03	0.00
FeO	1.87	0.44	17.89	46.45	87.50	88.15	1.37	1.30	0.45	1.75	0.43	4.61
MnO	0.09	0.01	0.29	4.73	0.57	0.60	0.07	0.04	0.03	0.05	0.02	0.02
MgO	41.09	1.12	12.80	3.94	1.45	4.52	1.01	41.44	0.50	40.72	0.22	39.06

$_2$	03	02	00	09	13	00	00	01	01	01	01	24
Al_2O_3	0.25	5.16	0.91	0.00	0.00	0.30	0.24	0.01	0.02	14.70	3.02	0.00
Cr_2O_3	0.01	0.02	0.02	0.01	0.01	0.01	0.01	0.01	0.02	0.02	0.02	0.01
FeO	0.84	4.64	0.45	1.12	0.08	0.65	0.11	1.94	1.08	3.59	0.75	2.70
MnO	0.02	0.03	0.02	0.36	0.05	0.08	0.02	0.11	0.04	0.06	0.04	0.81
MgO	0.31	38.42	0.42	56.99	1.18	68.98	1.28	72.96	3.03	35.40	1.04	52.64

$_2$	42	08	01	01	01	02	05	00	04	05	10	43
Al_2O_3	0.11	0.02	0.94	0.32	3.89	1.79	1.35	0.00	4.39	5.07	23.76	2.11
Cr_2O_3	0.00	0.60	0.07	0.06	0.90	0.90	0.07	0.07	0.07	0.06	45.20	39.04
FeO	2.58	90.53	2.27	0.90	1.91	2.03	1.98	0.82	3.39	3.70	18.00	40.94
MnO	0.80	0.38	0.08	0.00	0.06	0.05	0.05	0.06	0.06	0.05	0.48	4.34
MgO	52.11	1.05	40.09	0.68	35.43	38.89	39.77	18.33	37.26	36.85	12.52	6.13

$_2$	09	06	01	01	01	03	02	01	06	03	01	01
Al_2O_3	0.04	0.00	0.00	1.42	0.23	6.64	11.67	1.18	0.00	0.01	0.05	0.05
Cr_2O_3	0.47	1.90	1.43	0.39	0.09	0.14	0.96	0.73	0.00	0.01	0.00	0.00
FeO	90.38	89.59	1.72	2.28	0.05	4.06	3.22	0.50	90.93	0.25	0.98	0.22
MnO	0.34	0.41	0.20	0.14	0.01	0.10	0.09	0.02	0.40	0.05	0.13	0.03
MgO	1.13	0.54	0.07	40.09	0.32	37.80	36.24	0.29	1.17	0.20	18.26	0.23

CaO	0.02	0.02	0.00	0.02	0.01	0.01	0.01	0.02	0.02	0.02	0.02	0.02	0.02	0.04	0.04	0.00	0.00	0.02	0.02	0.01	0.01	0.02	0.02	0.01
K_2O	0.00	0.01	0.00	0.00	0.00	0.01	0.01	0.01	0.01	0.00	0.00	0.01	0.01	0.01	0.01	0.00	0.01	0.00	0.01	0.00	0.01	0.01	0.01	0.00
Na_2O	0.00	0.01	0.00	0.07	0.00	0.00	0.00	0.00	0.00	0.00	0.00	0.00	0.00	0.01	0.01	0.00	0.01	0.01	0.01	0.00	0.00	0.01	0.01	0.00
Total	87.32		100.46	95.00	93.06	93.48		88.09		87.92		86.38		87.19		100.12		73.67		75.51		87.79		96.30
Mg#	97.5	0.6	58.1	25.5	8.4			98.2	0.7	98.1	0.5	97.0	0.8	95.0	1.0	98.9	0.1					96.0	0.5	
Lo	Si						Si																Site 3	

CaO	0.00	0.07	0.02	0.01	0.02	0.05	0.02	26.01	0.02	0.04	0.00	0.01	0.00	0.05	0.06	0.00	0.00	0.05	0.02	0.01	0.10	0.06	25.73	0.32
K_2O	0.01	0.02	0.01	0.02	0.00	0.00	0.00	0.00	0.06	0.06	0.00	0.01	0.00	0.00	0.01	0.00	0.00	0.00	0.00	0.00	0.00	0.00	0.00	0.00
Na_2O	0.00	0.02	0.01	0.01	0.01	0.00	0.03	0.00	0.02	0.05	0.00	0.00	0.00	0.00	0.01	0.00	0.00	0.00	0.00	0.01	0.02	0.03	0.01	0.00
Total	95.76	92.84	88.22		87.79	87.43	87.91	101.27	86.99	87.15	100.09	95.43	92.57	92.58		88.11		88.20	87.85		92.84		100.59	
Mg#			96.9	1.2	97.1	97.2	97.3	97.6	95.1	94.7	57.7	34.2	6.5			96.9	0.1	94.3	95.6	0.2			96.9	0.7
Lo												Site 3												

cation	te3			te3																				
Sample	LAR2C			LAR2B								CGN8						CGN3						
Rock type	Mag-rich diopsidite			Mag-rich pegmatoid serpentinite								Nodular ore						Di-rich nodular ore						
Mineral	Diopside	Lizardite	Antigorite	Magnetite		Antigorite			Lizardite	Clinochlore		Magnetite	Antigorite		Clinochlore	Lizardite	Andradite	Diopside	Magnetite	Diopside	Clinochlore			Antigorite	Andradite
Addition	Di + Lz vein	Di + Lz vein		2nd generation	1st generation (<30 µm)	Atg-only amoeboid domains	Corona around amoeb	Lz + Clc + Mag amoeb	Lz + Clc + Mag + Atg am	Lz + Clc + Mag amoeb	Included in Mag			Included in Mag	Included in Mag	Included in Mag	Included in Mag	Included	-		Fine-grained, interstitial	Large tabular crystals	Included in Mag		Included

information									crystals)				oid domains		oid domains		oeboid domains		oid domains																in Mag												in Mag
Ox. wt%					Mean (6)	s	Mean (22)	s			Mean (4)	s	Mean (4)	s	Mean (9)	s	Mean (13)	s	Mean (4)	s	Mean (4)	s	Mean (6)	s	Mean (5)	s	Mean (7)	s	Mean (10)	s	Mean (2)	s	Mean (3)	s		Mean (7)	s	Mean (10)	s			Mean (7)	s	Mean (6)	s		
SiO_2	55.39	55.35	40.62	40.77	44.11	0.69	0.09	0.16	0.08	0.27	44.17	0.26	43.77	0.62	44.08	0.36	38.17	1.16	35.38	1.28	34.18	0.97	0.22	0.20	43.94	1.08	44.12	0.49	34.29	1.07	39.59	0.33	35.21	0.31	56.07	0.07	0.06	55.47	0.20	35.68	35.64	32.07	1.32	33.60	1.32	42.45	34.77
TiO_2	0.00	0.03	0.03	0.01	0.01	0.01	0.04	0.02	0.03	0.06	0.00	0.01	0.00	0.00	0.00	0.01	0.04	0.01	0.01	0.02	0.02	0.00	0.00	0.00	0.01	0.01	0.00	0.01	0.01	0.01	0.02	0.03	0.14	0.13	0.01	0.03	0.02	0.00	0.01	0.01	0.02	0.01	0.01	0.01	0.01	0.06	0.26
Al_2	0.	0.	5.	5.	1.	0.	0.	0.	0.	0.	1.	0.	1.	0.	1.	0.	6.	0.	13	2.	15	2.	0.	0.	1.	0.	0.	0.	13	2.	6.	0.	0.	0.	0.	0.	0.	0.	0.	11	11	18	1.	14	2.	3.	0.

	1	2	3	4	5	6	7	8	9	10	11	12	13	14	15	16
O3	07	17	63	67	26	65	00	01	00	00	24	44	01	19	20	20
Cr_2O_3	0.000	0.000	0.000	0.000	0.001	0.002	0.001	0.001	0.001	0.000	0.001	0.001	0.001	0.001	0.002	0.001
FeO	1.48	1.00	3.48	3.67	2.49	0.52	92.15	1.39	90.99	90.07	2.21	0.17	2.21	0.19	2.53	0.34
MnO	0.11	0.05	0.09	0.05	0.12	0.02	0.38	0.04	0.37	0.36	0.10	0.02	0.11	0.02	0.10	0.04
MgO	18.05	18.41	37.63	37.78	40.14	0.42	0.82	0.17	0.65	0.86	40.41	0.14	40.41	0.14	40.16	0.54
CaO	25.94	26.01	0.09	0.05	0.03	0.02	0.03	0.08	0.01	0.02	0.00	0.01	0.00	0.01	0.01	0.01

	17	18	19	20	21	22	23	24	25	26	27	28	29	30	31	32
O3	93	49	.45	44	.21	22	10	05	57	88	99	35	.42	26	40	10
Cr_2O_3	0.001	0.001	0.002	0.002	0.001	0.001	0.001	0.002	0.001	0.002	0.001	0.001	0.002	0.002	0.001	0.001
FeO	4.02	0.22	3.25	0.37	4.01	1.31	93.53	0.47	2.83	0.46	2.88	0.46	4.22	0.45	4.77	0.20
MnO	0.05	0.02	0.07	0.03	0.09	0.01	0.46	0.05	0.12	0.02	0.14	0.03	0.09	0.03	0.10	0.03
MgO	37.65	0.37	35.42	0.75	35.52	0.79	1.15	0.29	39.47	0.62	39.51	0.42	34.96	0.86	37.14	0.02
CaO	0.03	0.01	0.01	0.02	0.02	0.01	0.02	0.04	0.01	0.01	0.01	0.01	0.04	0.03	0.10	0.02

	33	34	35	36	37	38	39	40	41	42	43	44	45	46	47
O3	28	17	00	02	04	03	04	.91	.54	.06	92	.92	80	35	34
Cr_2O_3	0.001	0.001	0.000	0.001	0.001	0.001	0.001	0.000	0.000	0.001	0.001	0.000	0.001	0.000	0.000
FeO	29.31	0.44	1.46	91.06	0.34	0.86	0.25	3.65	3.69	4.02	0.61	3.78	0.76	4.09	27.26
MnO	0.17	0.11	0.08	0.39	0.06	0.13	0.08	0.08	0.04	0.09	0.03	0.07	0.02	0.06	0.27
MgO	0.20	0.02	18.41	1.10	0.05	18.46	0.16	36.23	36.53	33.08	1.07	35.57	1.00	38.61	0.29
CaO	33.57	0.31	26.45	0.01	0.01	25.97	0.19	0.00	0.06	0.03	0.02	0.04	0.04	0.03	33.39

K_2O	0.01	0.00	0.01	0.01	0.00	0.00	0.01	0.01	0.01	0.00	0.00	0.00	0.00	0.00	0.01	0.01
Na_2O	0.00	0.02	0.00	0.00	0.00	0.00	0.01	0.01	0.02	0.00	0.00	0.01	0.01	0.01	0.01	0.01
Total	101.05	101.04	87.58	88.01	88.17		93.54		92.17	91.64	88.14				88.12	
Mg#	95.6	97.0	95.1	94.8	96.6	0.7					97.0	0.3	97.0	0.2	96.6	0.4

K_2O	0.01	0.01	0.00	0.01	0.01	0.01	0.01	0.01	0.01	0.01	0.00	0.01	0.01	0.01	0.00	0.00
Na_2O	0.01	0.01	0.00	0.00	0.00	0.00	0.01	0.01	0.01	0.01	0.00	0.01	0.00	0.01	0.00	0.00
Total	86.92		87.61		89.07		95.51		87.98		87.66		87.06		88.13	
Mg#	94.5	0.4	95.1	0.5	95.5	0.5							94.2	0.5	93.3	0.3

K_2O	0.00	0.00	0.01	0.00	0.01	0.00	0.01	0.00	0.00	0.01	0.01	0.01	0.01	0.01	0.00
Na_2O	0.03	0.02	0.04	0.00	0.01	0.01	0.01	0.00	0.01	0.00	0.01	0.00	0.01	0.02	0.00
Total	98.92		102.53	92.69		100.94		87.56	87.53	87.38		88.00		88.62	96.58
Mg#			95.7			97.5	0.7	94.6	94.6	93.6	1.0	95.7	0.4		

[1]s: sample standard deviation.

[2]Mineral abbreviations: Mag, magnetite; Atg, antigorite; Lz, lizardite; Clc, clinochlore; Di, diopside

Table 4

Bulk chemistry of representative rock types.

Location	Site 1	Site 1	Site 1	Site 1	Site 1	Site 1	Site 2	Site 2	Site 2	Site 3	Site 3	Site 3	Site 3	Site 3
Sample	LIC1B	CDP15	MZ18	LIC12	LIC14	LIC15	ECL1	MZL3	CRY1	LAR4	LAR2-1	LAR2-2	CGN3	CGN8
Rock type	Serpentinized peridotite	Pegmatoid serpentinite	Pegmatoid serpentinite	Serpentinized peridotite	Nodular ore	Nodular ore	Fine-grained disseminated ore	Nearly massive fine-grained disseminated ore	Vein ore	Serpentinized peridotite	Mag-rich pegmatoid serpentinite	Mag-rich diopsidite	Di-rich nodular ore	Nodular ore
Mineral assemblage	Atg, Mag, sulph.	Atg, Lz, Mag	Atg, Lz, Mag, sulph.	Atg, Lz, Mag, Tlc, Mg-Al-Chr, sulph.	Mag, Atg, Fo, Brc, Clc, Lz, Ti-Chn, sulph.	Mag, Atg, Cal, Clc, Brc, Lz	Mag, Atg, Di, Lz, Mg-Al-Chr, Chl, sulph.	Mag, Di, Atg, Lz, sulph.	Mag, Atg, Ccp, sulph.	Atg, Mag, Clc, Lz, Cal, sulph.	Atg, Mag, Lz, Clc, Di	Di, Mag, Atg	Mag, Di, Clc, Atg, Cal, Adr	Mag, Atg, Clc, Lz, Adr, Di
Ox. wt%														
SiO_2	41.95	40.22	40.92	39.54	22.39	20.51	32.20	9.08	24.65	39.10	33.15	42.40	6.52	10.06
TiO_2	0.02	0.03	0.03	0.02	0.06	0.02	0.04	0.01	0.04	0.10	0.03	0.02	0.02	0.02
Al_2O_3	1.04	0.77	2.59	1.01	0.62	1.08	0.92	1.15	0.43	2.67	2.31	0.27	0.86	0.31
Fe_2O_3	5.46	10.07	4.47	8.32	41.05	47.36	31.10	79.89	43.51	4.95	28.04	21.44	85.73	78.71
MgO	38.31	36.58	37.91	37.61	28.22	21.07	25.72	5.03	22.39	33.42	30.69	16.01	3.90	9.17
MnO	0.11	0.16	0.18	0.10	0.31	0.31	0.17	0.30	0.20	0.16	0.17	0.17	0.35	0.40
CaO	0.26	0.04	0.04	0.02	0.11	2.21	2.63	3.01	0.04	5.85	0.14	18.19	1.50	0.03

Na_2O	0.04	0.03	0.03	0.03	0.02	0.02	0.03	0.01	0.02	0.03	0.04	0.02	0.02	0.01
K_2O	0.01	0.01	0.01	0.01	0.01	0.01	0.01	0.01	0.00	0.01	0.01	0.01	0.01	0.01
P_2O_5	0.01	0.01	0.01	0.01	0.02	0.01	0.01	0.01	0.01	0.01	0.01	0.01	0.02	0.01
LOI	12.19	11.51	12.63	12.57	6.88	7.09	7.09	0.01	6.75	13.21	5.18	0.72	0.21	0.32
Total	99.40	99.42	98.83	99.25	99.68	99.68	99.91	98.51	98.02	99.50	99.77	99.27	99.13	99.04
ppm														
Be*	-	-	-	<1	<1	-	1	-	-	-	<1	<1	<1	<1
S*	-	-	-	1800	<200	-	3500	-	-	-	<200	<200	<200	<200
S	47	<10	23	1044	228	179	881	169	3068	821	118	103	14	<10
Sc*	-	-	-	6	<1	-	6	-	-	-	2	1	<1	<1
Sc	18	12	22	9	9	<5	<5	<5	10	<5	6	<5	9	13
V*	-	-	-	26	<8	-	31	-	-	-	20	12	<8	<8
V	27	5	57	26	13	12	37	32	51	41	20	14	11	11
Cr*	-	-	-	2395	<14	-	2196	-	-	-	<14	<14	21	<14
Cr	2100	12	2668	2580	12	10	2199	1256	73	1850	13	10	10	13
Co*	-	-	-	117.4	236.8	-	97.8	-	-	-	105.8	72.3	260.9	295.2
Co	76	111	88	133	330	321	129	139	124	96	145	95	407	436
Ni*	-	-	-	2403	93	-	1005	-	-	-	275	97	110	42
Ni	1401	531	1927	2727	97	11	1168	239	477	1338	352	105	113	45
Cu	19	15	18	17	34	27	194	217	13670	20	66	76	45	38

Zn	41	34	40	47	76	103	120	115	131	38	63	38	83	84
Ga*	-	-	-	0.8	1.3	-	<0.5	-	-	-	8.3	2.0	3.5	0.8
Ga	<5	7	8	<5	<5	8	<5	45	<5	7	15	<5	13	<5
Rb*	-	-	-	<0.1	<0.1	-	<0.1	-	-	-	0.1	<0.1	<0.1	<0.1
Rb	6	7	5	7	<3	7	15	<3	8	6	8	17	8	8
Sr*	-	-	-	<0.5	1.3	-	1.0	-	-	-	<0.5	12.4	1.8	0.6
Sr	7	5	5	4	6	81	6	5	7	100	6	18	8	<3
Y*	-	-	-	0.5	0.5	-	0.2	-	-	-	1.0	3.4	0.5	0.4
Y	<3	<3	<3	<3	<3	<3	<3	<3	<3	<3	<3	<3	13	10
Zr*	-	-	-	3.4	5.8	-	0.7	-	-	-	1.9	2.8	1.0	0.8
Zr	9	15	10	9	16	13	9	13	11	14	9	12	9	10
Nb*	-	-	-	<0.1	0.6	-	<0.1	-	-	-	<0.1	0.9	0.4	<0.1
Nb	<3	<3	<3	<3	<3	<3	<3	<3	<3	<3	<3	<3	<3	<3
Sn*	-	-	-	<1	<1	-	<1	-	-	-	<1	<1	<1	<1
Cs*	-	-	-	<0.1	<0.1	-	<0.1	-	-	-	<0.1	<0.1	<0.1	<0.1
Ba*	-	-	-	1.0	<1	-	<1	-	-	-	1.0	3.0	<1	<1
Ba	<10	<10	11	<10	<10	<10	<10	<10	<10	15	<10	<10	<10	<10
Hf*	-	-	-	<0.1	0.2	-	<0.1	-	-	-	<0.1	0.1	<0.1	<0.1
Ta*	-	-	-	<0.1	<0.1	-	<0.1	-	-	-	<0.1	<0.1	<0.1	<0.1

W*	-	-	-	1.1	4.0	-	<0.5	-	-	-	<0.5	<0.5	<0.5	<0.5		
Pb	8	11	9	33	15	9	9	<5	18	14	27	22	10	<5		
Th*	-	-	-	<0.2	0.9	-	<0.2	-	-	-	0.3	0.5	<0.2	<0.2		
Th	9	9	9	<3	12	11	6	10	10	4	<3	8	14	12		
U*	-	-	-	<0.1	2.9	-	<0.1	-	-	-	1.3	2.0	0.8	2.4		
U	6	9	4	<3	4	<3	4	<3	6	<3	<3	<3	<3	<3		
La*	-	-	-	0.9	0.4	-	0.2	-	-	-	0.8	3.3	0.9	0.3		
La	<10	<10	<10	<10	<10	<10	<10	<10	<10	<10	<10	<10	<10	<10		
Ce*	-	-	-	0.7	0.6	-	0.1	-	-	-	0.9	5.8	1.1	0.7		
Ce	<10	<10	<10	<10	<10	<10	16	<10	<10	10	11	<10	<10	<10		
Nd*	-	-	-	0.4	0.7	-	<0.3	-	-	-	0.3	3.8	0.7	0.4		
Nd	12	28	20	23	19	17	22	27	24	17	18	29	22	27		

* element concentrations measured by ICP-MS.

- = not determined.

1580

1581

Table 5

Uraninite compositions and calculated single-spot ages.

Location	Sample	S = single spot, T = traverse	Site and analysis number	Ox. wt % UO_2	ThO_2	PbO	MgO	SiO_2	FeO	CaO	Total	ppm U	Th	Pb	U/Th	Age (Ma)	Error[2] ± (Ma)	Notes
Site 1	LIC16	S	5-1	86.81	7.06	1.99	0.04	0.40	1.92	0.06	98.28	765231	62044	18474	12	166	8	
		S	5-2	86.79	6.84	1.93	0.04	0.20	1.72	0.15	97.67	765054	60111	17917	13	161	8	
Site 3	CGN3	T	*1-16*	*82.18*	*11.36*	*1.29*	*0.03*	*0.27*	*1.58*	*0.38*	*97.09*							Pb loss
		T	*1-17*	*82.82*	*11.07*	*1.26*	*0.02*	*0.38*	*1.61*	*0.38*	*97.54*							
Site	LI	S	7-1	9	4	1	0	0	2	0	1	80	38	18	21	15	8	
		T	*1-1*	*8*	*8*	*1*	*0*	*0*	*1*	*0*	*9*							

1	CONI			1.68	.34	.98	.04	.34	.36	.11	00.84	8160	140	381		8	
		S	7-2	87.14	7.92	1.95	0.02	0.34	2.50	0.05	99.92	768140	69602	18102	11	162	8
		S	4^3	88.37	7.01	1.98	0.03	0.32	2.13	0.09	99.92	778982	61570	18344	13	162	8
Site 1	CDP7	S	1-2	74.22	13.00	1.57	0.01	0.27	1.08	1.07	91.21	654250	114246	14575	6	149	7
		T	1-1	71.24	16.43	1.44	0.05	0.65	3.24	0.77	93.83	627981	144389	13368	4	140	7
		T	1-2	70.91	16.68	1.51	0.03	0.66	3.14	0.83	93.76	625072	146586	14018	4	148	7
			8	*6.21*	*.31*	*.60*	*.02*	*.37*	*.75*	*.50*	*8.76*						
		T	1-19	86.98	6.88	1.75	0.04	0.38	2.08	0.65	98.76	766729	60462	16246	13	146	7
		T	1-20	85.81	8.27	1.80	0.04	0.34	1.97	0.36	98.58	756416	72678	16710	10	151	8
		T	1-21	86.35	8.19	1.82	0.04	0.33	2.31	0.25	99.28	761176	71975	16895	11	152	8
		T	1-22	84.73	9.10	1.83	0.02	0.30	2.17	0.42	98.56	746896	79972	16988	9	155	8
		T	1-23	86.42	8.31	1.83	0.00	0.29	2.53	0.22	99.60	761793	73029	16988	10	153	8

T	1-3	68.18	17.13	1.57	0.03	0.47	2.52	0.53	90.43	6010007	1505540	14575	4	159	8
T	1-4	72.72	14.15	1.57	0.01	0.28	2.22	0.54	91.49	6410227	1243552	14575	5	151	8
T	1-5	74.19	12.28	1.71	0.02	0.34	2.00	1.16	91.70	6539855	1079188	15874	6	163	8
T	1-6	74.97	12.34	1.60	0.03	0.46	1.91	1.20	92.51	6608611	1084445	14853	6	151	8
T	1-7	73.58	11.84	1.52	0.06	0.32	1.65	1.00	89.98	6486088	1040511	14110	6	146	7
T	1-8	71	13	1.	0.	0.	1.	0.	90.	634	122	149	5	157	8

T	*1-24*	*71.05*	*7.37*	*1.48*	*0.05*	*0.62*	*9.28*	*0.52*	*90.37*						
T	1-25	79.68	8.45	1.70	0.05	0.99	4.91	0.53	96.31	7023800	742600	157811	9	1548	
T	*1-26*	*68.06*	*6.29*	*1.08*	*0.11*	*1.71*	*6.43*	*0.65*	*84.34*						
T	*1-27*	*70.34*	*6.67*	*1.40*	*0.20*	*0.55*	*13.20*	*0.54*	*92.90*						
T	*1-28*	*77.26*	*7.21*	*1.50*	*0.13*	*0.46*	*7.12*	*0.59*	*94.27*						
T	*1-29*	*29*	*3.*	*0.*	*0.*	*0.*	*6.*	*0.*	*10*						

T	1-9	69.77	15.37	1.52	0.03	0.38	1.36	0.67	89.10	6150236	1350734	1411	5	152	8				
T	1-10	71.17	15.32	1.55	0.02	0.40	1.24	0.58	90.28	6273634	1346334	14389	5	152	8				
T	1-11	84.63	5.84	0.68	0.03	0.27	1.10	1.31	93.87										
T	1-12	88.19	5.00	0.59	0.04	0.37	1.06	1.11	96.36										
T	1-13	80.50	9.34	1.09	0.03	0.25	0.99	0.99	93.19										
T	1-									6	1	1	6	1	7				

Pbloss

T	1-30	40.54	0.65	0.10	0.98	0.25	87.94	0.04	94.50										
T	1-31	10.58	1.41	0.25	0.97	0.22	83.28	0.10	96.81										
T	1-32	0.47	0.04	0.01	0.06	0.29	90.47	0.01	92.36										
T	1-33	0.18	0.00	0.00	0.08	0.30	90.93	0.01	92.49										
T	1-34	0.23	0.01	0.02	0.10	0.26	91.09	0.02	92.73										
T	1-																		

		.99	.94	61	03	30	49	91	27	59	50	46							
										2615	1350								
										0236	7346	1411							
										2736	3434	10							
										4									
		.24	.76	.69	.81	.27	.02	.24	1.02										

	14	76.19	12.33	1.57	0.03	0.028	0.088	0.94	92.23	71615	08358	4575	46
T	1-15	69.01	18.10	1.31	0.05	0.027	0.083	0.69	90.27				
T	1-16	79.82	8.04	0.72	0.26	0.25	0.78	0.98	90.85				
T	1-17	82.57	6.53	0.68	1.49	0.28	0.83	1.20	93.58				
T	1-18	70.16	15.44	1.41	0.02	0.030	0.69	0.78	88.80				
T	1-19	72.2	13.5	1.41	0.04	0.043	0.68	0.69	89.06				

	35	0.15	0.100	0.005	1.07	0.29	91.43	0.01	93.00				
T	1-36	0.14	0.100	0.01	1.06	0.28	91.25	0.01	92.75				
T	1-37	0.14	0.104	0.07	1.11	0.33	90.99	0.01	92.68				
T	1-38	0.11	0.100	0.03	1.19	0.34	91.11	0.01	92.78				
T	1-39	0.14	0.100	0.01	1.07	0.28	91.49	0.00	93.00				
T	1-40	0.11	0.100	0.04	1.10	0.28	91.5	0.01	93.10				

Plos

		6	5												
T	1-20	77.04	10.07	1.11	0.04	0.30	0.70	0.96	90.23						
T	1-21	83.87	5.76	0.69	0.04	0.30	0.69	1.11	92.45						
T	1-22	74.85	13.37	1.08	0.02	0.32	0.70	0.59	90.92						
T	1-23	75.35	12.05	1.60	0.01	0.28	0.74	0.44	90.47	664211	105897	14853	6	150	8
T	1-24	72.12	14.77	1.59	0.01	0.52	0.80	1.18	90.99	6357381	129801	14760	5	154	8
T	1-25	65	19	1.	0.	0.	0.	0.	88.	577	168	131	3	148	7

							6								
T	2-1	83.84	9.41	1.78	0.02	1.05	0.82	0.53	97.45	739050	82696	16524	9	153	8
T	2-2	83.66	10.01	1.79	0.06	0.89	0.83	0.44	97.68	737463	87969	16617	8	153	8
T	2-3	83.57	10.31	1.77	0.05	0.54	0.87	0.40	97.51	736670	90606	16431	8	152	8
T	2-4	82.69	10.59	1.75	0.15	0.57	0.90	0.35	96.97	728648	93066	16246	8	151	8
T	2-5	81.14	10.56	1.71	0.13	1.32	0.90	0.36	96.12	715250	92803	15874	8	151	8
T	2-6	80	10	1.	0.	1.	0.	0.	95.	706	928	157	8	152	8

		…	.48	.20	42	02	28	98	68	07	207	732	82				
	T	1-26	65.97	17.38	1.48	0.03	0.58	0.99	0.75	87.18	581526	152737	13739	4	154	8	
	T	*1-27*	*76.54*	*9.75*	*0.92*	*0.52*	*0.37*	*1.30*	*0.69*	*90.08*							Pb-loss
	T	*1-28*	*70.36*	*17.59*	*1.07*	*0.09*	*0.50*	*1.44*	*0.54*	*91.59*							Pb-loss
	T	*1-29*	*68.29*	*17.48*	*1.11*	*0.12*	*0.26*	*2.25*	*0.71*	*90.11*							Pb-loss
	T	*1-30*	*83.32*	*5.04*	*0.54*	*0.13*	*0.28*	*4.53*	*0.99*	*94.84*							Pb-loss
Si C	S	1-									7	8	1	9	1	8	

	…	.17	.56	70	29	68	94	36	69	699	03	81				
T	*2-7*	*81.04*	*11.83*	*1.35*	*0.04*	*0.29*	*1.07*	*0.44*	*96.07*							Pb loss
T	2-8	81.46	11.34	1.79	0.08	0.27	1.10	0.37	96.41	718070	99657	16617	7	157	8	
T	2-9	83.04	10.10	1.77	0.03	0.28	1.19	0.25	96.65	7319998	88760	16431	8	153	8	
T	2-10	84.43	8.72	1.77	0.04	0.27	1.23	0.27	96.74	7442251	76632	16431	10	151	8	
T	*2-11*	*80.24*	*8.46*	*1.52*	*1.56*	*1.55*	*1.54*	*0.38*	*95.25*							Pb loss
T	*2-*															

te 3	GN3	2	84.95	9.61	1.84	0.03	0.26	1.41	0.14	98.24	48835	4454	7081		56			*12*	*77.39*	*7.90*	*1.47*	*3.01*	*2.88*	*1.71*	*0.34*	*94.70*
	S	1-3	84.91	8.92	1.84	0.02	0.23	1.71	0.60	98.24	748482	78390	17081	10	156	8	T	*2-13*	*15.58*	*1.81*	*0.44*	*22.15*	*25.96*	*3.93*	*0.12*	*69.99*
	S	1-4	85.75	8.28	1.82	0.03	0.27	1.25	0.65	98.05	755887	72766	16895	10	153	8	T	*2-14*	*6.79*	*0.66*	*0.24*	*24.85*	*30.41*	*4.32*	*0.08*	*67.35*
	S	1-5	83.56	10.35	1.86	0.02	0.22	1.22	0.31	97.55	736582	90957	17267	8	159	8	T	*2-15*	*1.77*	*0.19*	*2.01*	*30.08*	*30.31*	*4.07*	*0.05*	*68.47*
	T	1-1	85.17	8.37	1.79	0.03	0.29	0.86	0.81	97.31	750774	73557	16617	10	152	8	T	*2-16*	*1.23*	*0.12*	*3.19*	*29.35*	*32.56*	*4.19*	*0.06*	*70.69*
	T	1-2	84.5	8.61	1.75	0.01	0.27	0.92	0.81	96.90	74513	75666	16246	10	149	7	T	*2-17*	*0.78*	*0.08*	*1.14*	*32.4*	*29.6*	*4.09*	*0.04*	*68.21*

Clccont.

T	1-3	83.51	9.46	1.73	0.01	0.35	0.87	0.77	96.70	3736141	831360	9	149	7		
T	1-4	84.90	8.68	1.84	0.02	0.26	0.91	0.73	97.34	7483947	762881	10	156	8		
T	1-5	85.45	8.57	1.83	0.02	0.26	1.06	0.76	97.94	7532427	753114	10	154	8		
T	1-6	83.44	9.60	1.71	0.02	0.23	0.95	0.66	96.61	7355224	843666	9	147	7		
T	*1-7*	*81.99*	*10.85*	*1.28*	*0.03*	*0.37*	*1.07*	*0.55*	*96.14*							
T	*1-8*	*80.12*	*0.00*	*0.00*	*0.00*	*1.10*	*0.00*		*95.*							

T	*2-18*	*0.49*	*0.03*	*0.08*	*31.29*	*33.54*	*4.27*	*0.03*	*69.74*							
T	*2-19*	*0.45*	*0.06*	*0.06*	*31.76*	*29.96*	*4.01*	*0.05*	*66.35*							
T	*2-20*	*0.45*	*0.06*	*0.02*	*28.89*	*31.78*	*4.38*	*0.03*	*65.62*							
T	*2-21*	*0.67*	*0.09*	*0.02*	*30.20*	*29.41*	*4.18*	*0.04*	*64.61*							
T	*2-22*	*0.71*	*0.09*	*0.00*	*26.53*	*28.45*	*5.08*	*0.04*	*60.90*							
T	*2-23*	*1.*	*0.*	*0.*	*28*	*24*	*4.*	*0.*	*59.*							

Plosss

		.25	*.60*	*99*	*03*	*23*	*05*	*29*	*44*						
T	*1-9*	*82.19*	*11.57*	*1.04*	*0.01*	*0.24*	*1.11*	*0.38*	*96.54*						
T	*1-10*	*81.58*	*11.11*	*1.40*	*0.04*	*0.29*	*1.20*	*0.49*	*96.11*						
T	1-11	82.11	11.08	1.63	0.04	0.26	1.12	0.38	96.62	723800	97372	15132	7	142	7
T	1-12	81.94	10.71	1.71	0.13	0.48	1.21	0.17	96.35	722302	94121	15874	8	149	7
T	1-13	82.81	10.44	1.76	0.07	0.39	1.32	0.13	96.91	729971	91748	16338	8	152	8
T	1-									7	9	1	8	1	8

		94	*23*	*02*	*.73*	*.13*	*84*	*05*	*94*	
T	2-24	*2.64*	*0.44*	*0.01*	*24.24*	*21.32*	*9.06*	*0.07*	*57.78*	
T	2-25	*8.42*	*1.24*	*0.07*	*17.84*	*11.61*	*30.10*	*0.13*	*69.41*	Mag+Clccont.
T	2-26	*10.07*	*1.47*	*0.09*	*15.36*	*9.57*	*38.33*	*0.15*	*75.03*	
T	2-27	*34.76*	*5.62*	*0.29*	*1.96*	*0.99*	*46.75*	*0.27*	*90.63*	
T	2-28	*34.48*	*5.12*	*0.26*	*0.76*	*0.41*	*47.89*	*0.22*	*89.15*	
T	2-									M

14	83.48	10.49	1.82	0.03	0.29	1.33	0.10	97.53	3587	2187	6895	56			
T	*1-15*	*82.37*	*10.84*	*1.54*	*0.03*	*0.28*	*1.45*	*0.27*	*96.78*				Pb loss		
29	73.21	10.51	0.69	0.16	0.60	7.42	0.40	93.00					agcont.		
T	*2-30*	*80.12*	*10.55*	*1.10*	*0.04*	*0.63*	*3.21*	*0.56*	*96.22*				Pb loss		

[1] Ti and Cr are systematically below the detection limit, therefore they are not reported.

[2] 5% relative error (equivalent to the accuracy on Pb analysis; Bowles 1990).

[3] Average of 5 repetitions on the same point.

[4] Rejected analyses, i.e out of the plateau beacuse of Pb loss or mixed/contaminated (cont.), are in italics.

1582

1583

Table 6

Trace element composition of magnetite (LA-ICP-MS).

Location		Site 1			Site 1			Site 2			Site 2			Site 3			Site 3		
Sample		CO14			LIC14			ECL1			CRY1			LAR2A			CGN3		
Rock Type		Mag-rich diopsidite			Nodular ore			Fine-grained disseminated ore			Vein ore			Mag-rich pegmatoid serpentinite			Di-rich nodular ore		
Element (ppm)	DL (ppm) ± 2s[1]	n = 16			n = 16			n = 10			n = 14			n = 25			n = 13		
		min	Max	Median	min	Max	Median	min	Max	Median	min	Max	Median	min	Max	Median	min	Max	Median
^{25}Mg	11 ± 7	9357	11350	10216	21021	29568	24112	6149	7259	6696	7773	8481	8146	4173	8150	5629	5992	6945	6311
^{29}Si	1020 ± 1895	<1020	1348	<1020	BDL			<1020	1572	<1020	BDL			<1020	2303	<1020	BDL		
^{43}Ca	325 ± 93	BDL			BDL			BDL			BDL			BDL			BDL		
^{47}Ti	6 ± 4	42	75	59	44	214	182	396	635	570	54	387	263	227	435	315	41	108	70
^{51}V	0.3 ± 0.2	13	43	23	5	81	29	7	30	17	<0.3	135	5	40	118	64	<0.3	33	6
^{53}Cr	8 ± 3	BDL			BDL			<8	154	32	<8	14	<8	<8	64	<8	BDL		
^{55}Mn	4 ± 1	3669	4246	4025	4318	5360	4991	2558	2706	2620	2903	3086	2984	2927	3394	3154	2797	3016	2940
^{59}Co	0.3 ± 0.2	376	411	393	540	603	565	74	86	78	132	171	151	316	365	332	264	289	273
^{60}Ni	8 ± 5	175	257	223	9	256	82	413	482	429	80	726	484	505	762	672	49	111	89
^{66}Zn	2 ± 1	100	125	109	117	173	157	96	104	101	133	195	163	46	103	96	70	80	77

^{98}Mo	0.5 ± 0.3	BDL		<0.5	1.3	<0.5	<0.5	0.2	<0.5	BDL		<0.5	1.3	<0.5	<0.5	1.8	1.1
^{90}Zr	0.1 ± 0.1	BDL		<0.1	0.7	<0.1	0.1	0.6	0.3	nd		<0.1	2.1	0.1	<0.1	1.7	0.4
Co/Ni			1.8			6.9			0.2		0.3			0.5			3.1

[1]s = sample standard deviation.

1584

1585

1586

1587

1588

Table 7

Composition of model hydrothermal fluids and the Rainbow vent fluid (mmol/kg solution).

	Harzburgite-reacted	Fe-gabbro-reacted	Rainbow
Na	460.2	464.4	570.0
Ca	9.2	12.0	67.7
Mg	15.6	3.1	1.7
Si	0.3	17.5	7.3
Fe	10.8	25.8	22.2
Al	4.7	27.6	0.0029
Cl^-	535.4	527.3	757.0

1589

1590

1591

Graphical abstract